Supplementary Information for

A durable half-metallic diatomic catalyst for efficient oxygen reduction

Hongguan Li[1,2], Shuanlong Di[3], Ping Niu[1,2], Shulan Wang[3], Jing Wang[4]* & Li Li[1,2]*

1. School of Metallurgy, Northeastern University, Shenyang 110819, P. R. China.

2. State Key Laboratory of Rolling and Automation, Northeastern University, Shenyang 110819, Liaoning, P. R. China.

3. Department of Chemistry, College of Science, Northeastern University, Shenyang 110819, Liaoning, P. R. China.

4. Key Laboratory of Applied Chemistry in Hebei Province, Yanshan University, Qinhuangdao 066004, Hebei, P. R. China.

*Correspondence to: jwang6027@ysu.edu.cn (J. Wang); lilicmu@alumni.cmu.edu (L. L.)

This PDF file includes:

>   **Supplementary Text**
>
>   **Figures S1 to S57**
>
>   **Tables S1 to S19**
>
>   **References**

Supplementary Notes

Materials

Pt catalyst (20 % Pt supported on Vulcan XC-72 carbon) was commercially available (Johnson Matthey), and Nafion (5.0 wt. %) was purchased from Sigma-Aldrich. Deionized water was used in all experiments.

Characterization

The phase composition was verified with Rigaku D/MAX-2500 X-ray diffractometer using Cu Kα radiation ($\lambda = 0.154$ nm) at the scanning speed of 5° min^{-1} from 10° to 80°. Scanning electron microscopy (SEM, JSM-6700F) and transmission electron microscopy (TEM, JEM-2100F) were conducted to investigate the morphology and microstructure of samples. HAADF image was obtained by FEI Tecnai G2 F30 S-Twin operating at 300 kV and elemental mapping was achieved with energy dispersive X-ray spectrometer (EDS, Oxford). The surface area was measured through an American Micromeritics Tristar 3000 analyzer for recording N_2 adsorption/desorption isotherm at 77 K with pore size distribution obtained through the Barrett-Joyner-Halenda (BJH) model. Raman spectra were recorded on a Renishaw inVia Raman microscope (HR800, HORIBA Scientific) with an Ar-ion laser at the excitation wavelength of 514.5 nm. Inductively coupled plasma mass spectrometer (ICP-MS, Agilent 7500c) was used to check the elemental contents within the samples. The XAFS spectra at the Fe and Zn K-edge were recorded with Ge (220) and Si (111) double crystal monochromators and a Si drift detector for fluorescent X-rays while the acquired data were processed based on the standard procedures with the ATHENA module in the IFEFFIT software packages.

Electrochemical measurements

The electrochemical performance evaluation was carried out with the CHI 760E electrochemical workstation (Shanghai Chenhua) under a standard three-electrode system, including the glassy

carbon rotating ring-disk electrode (RRDE, PINE) as the working electrode, Hg/HgO (for 0.1 M KOH electrolyte) or Ag/AgCl (for 0.1 M HClO$_4$ electrolyte) as the reference electrode, and platinum foil (1 cm^2) as the counter electrode. The catalyst ink was prepared by ultrasonically mixing 5 mg samples with ethanol (800 μL), isopropanol (170 μL), and Nafion solution (30 μL, 5 wt. %) for 2 h. Correspondingly, Pt/C was prepared with the same protocol and used as the benchmark for ORR testing. 15 μL uniformly dispersed catalyst ink drops were coated on RRDE with a loading of 0.38 mg cm^{-2}. High purity N$_2$ or O$_2$ were purged into electrolytes for saturation before measurements. CV and LSV curves were measured at a sweep rate of 50 and 10 mV s^{-1} (at 0.3 ~ −0.8 V and 1 ~ −0.25 V), respectively. The electron transfer number was obtained by fitting the LSV curves at different speeds (400, 800, 1200, 1600 and 2000 rpm, respectively) through the Koutechy-Levich equation.[1] The stability test was performed by measuring the LSV curves of the electrode after 5000 CV cycles at a potential of 1 ~ −0.25 V in a 0.1 M HClO$_4$ electrolyte saturated with O$_2$.

Zinc–air battery assembly

The assembly of the liquid zinc-air battery: A polished zinc foil with a thickness of 0.3 mm is used as the anode. A mixed solution of 6 M KOH and zinc acetate was used as the electrolyte, and the carbon cloth supported catalyst (with a loading of 1.0 mg cm^{-2}) was used as the cathode.

The assembly of all solid-state zinc-air batteries: A polished zinc foil is used as anode, Fe/Zn-N-C catalyst supported on carbon cloth is used as air cathode and polyvinyl alcohol (PVA) is used as electrolyte, respectively. The PVA electrolyte gel is prepared as follows: 4.5 g PVA was firstly added to 45 mL deionized water with the stirring at 95°C for 1 hour, following with the addition of a mixed solution (5 mL) of 18 M KOH and 0.02 M zinc acetate. After stirring for another 1 hour, the gel was poured into a watch glass and frozen at −20°C for 24 hours.

DFT calculations

The computational simulations were conducted by VASP package,[2, 3] in which the PAW method[4] and the GGA-PBE approximation[5] were used to describe core-valence interactions. The specific calculation parameters are based on the previously reported execution.[6] A 5 × 5 graphene supercell was used with 15 Å vacuum along the c axis to avoid interactions between layers. The cutoff energy was set to be 500 eV. The Brillouin zone was sampled by the Monkhorst-Pack method with a 5 × 5 × 1 k-point grid. The energy convergence criteria is 10^{-5} eV and force certification is 0.01 eV A^{-1}. The van der Waals (vdW) interaction is involved via the semi-empirical DFT-D2 field method. The entropy and vibration frequency of the molecules in the gas phase are referred from the NIST database.
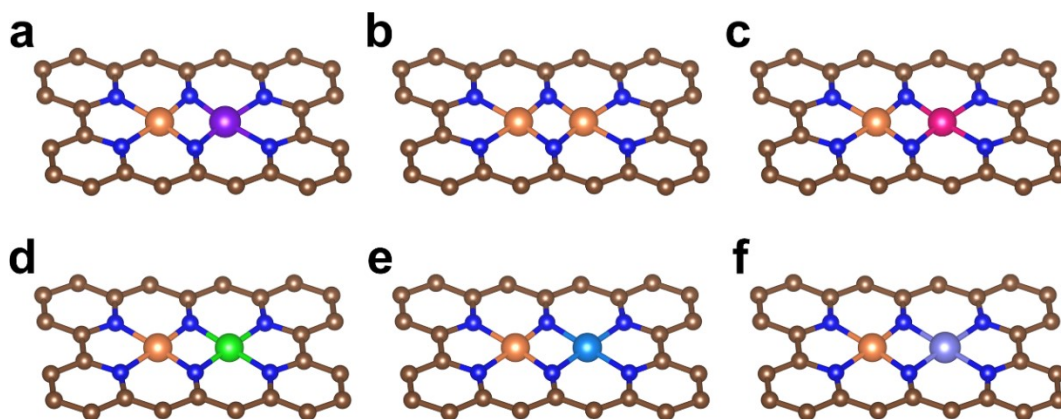
Figure S1. Six models of Fe/M-N-C (M=Mn, Fe, Co, Ni, Cu and Zn). (a) Fe/Mn-N-C, (b) Fe/Fe-N-C, (c) Fe/Co-N-C, (d) Fe/Ni-N-C, (e) Fe/Cu-N-C and (f) Fe/Zn-N-C.
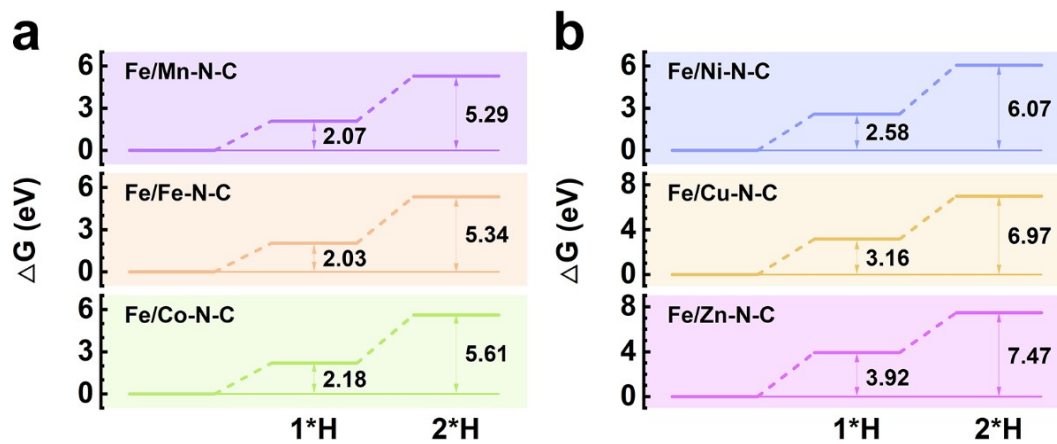
Figure S2. The free energy diagrams for 1*H and 2*H protonation based on the Fe/M-N-C structure. (a) Fe/Mn-N-C, Fe/Fe-N-C and Fe/Co-N-C, and (b) Fe/Ni-N-C, Fe/Cu-N-C and Fe/Zn-N-C, respectively.
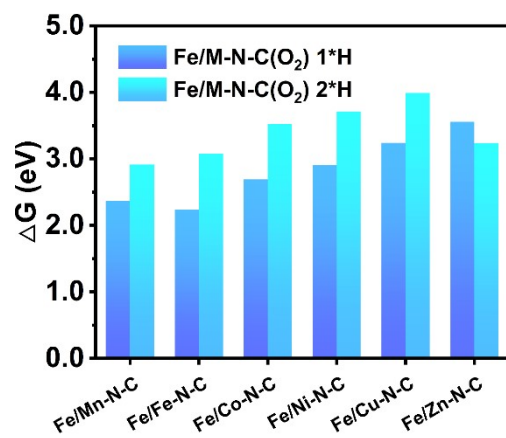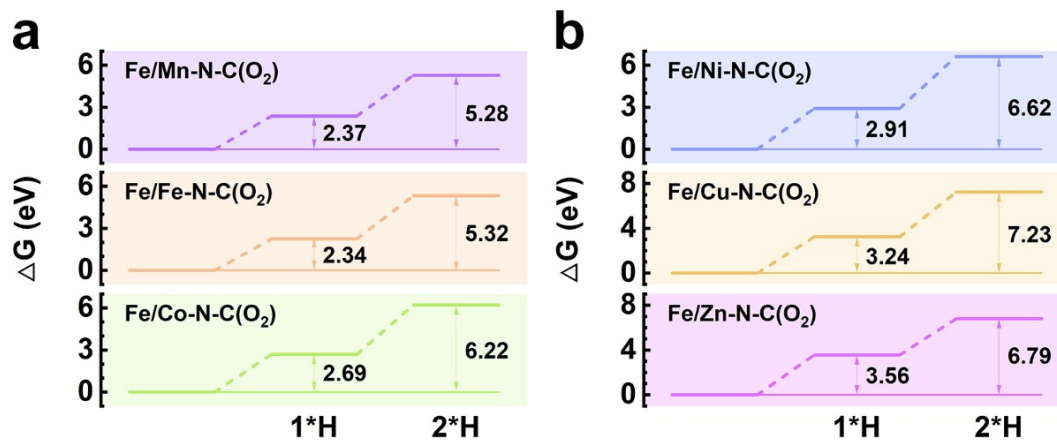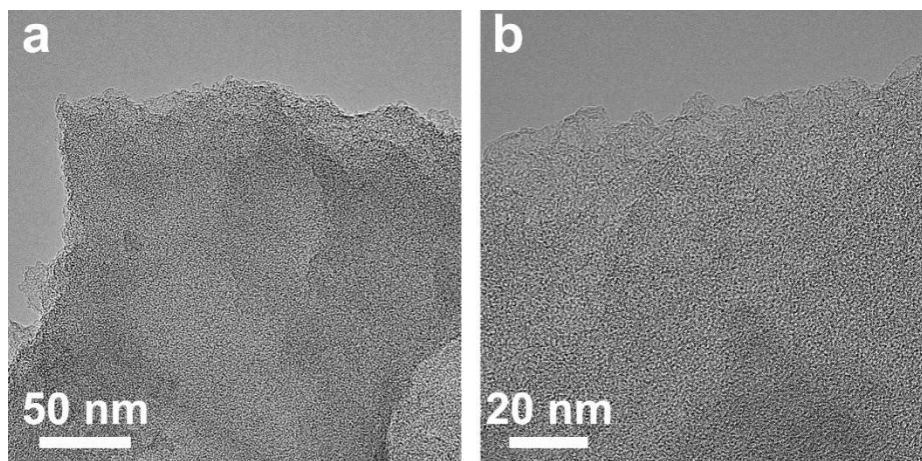
Figure S3. ΔG for 1*H and 2*H protonation of Fe/Mn-N-C(O_2), Fe/Fe-N-C(O_2), Fe/Co-N-C(O_2), Fe/Ni-N-C(O_2), Fe/Cu-N-C(O_2) and Fe/Zn-N-C(O_2).

Figure S4. The free energy diagrams for 1*H and 2*H protonation based on the Fe/M-N-C(O_2) structure. (a) Fe/Mn-N-C(O_2), Fe/Fe-N-C(O_2) and Fe/Co-N-C(O_2), and (b) Fe/Ni-N-C(O_2), Fe/Cu-N-C(O_2) and Fe/Zn-N-C(O_2), respectively.

Figure S5. TEM images of Fe/Zn-N-C under different magnifications. (a) The scale bar is 50 nm. (b) The scale bar is 20 nm.
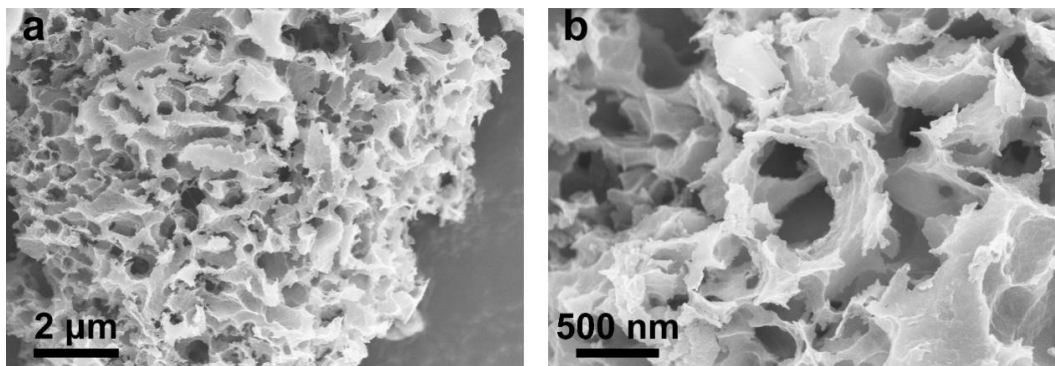
Figure S6. SEM images of Fe/Zn-N-C under different magnifications. (a) The scale bar is 2 μm. (b) The scale bar is 500 nm.
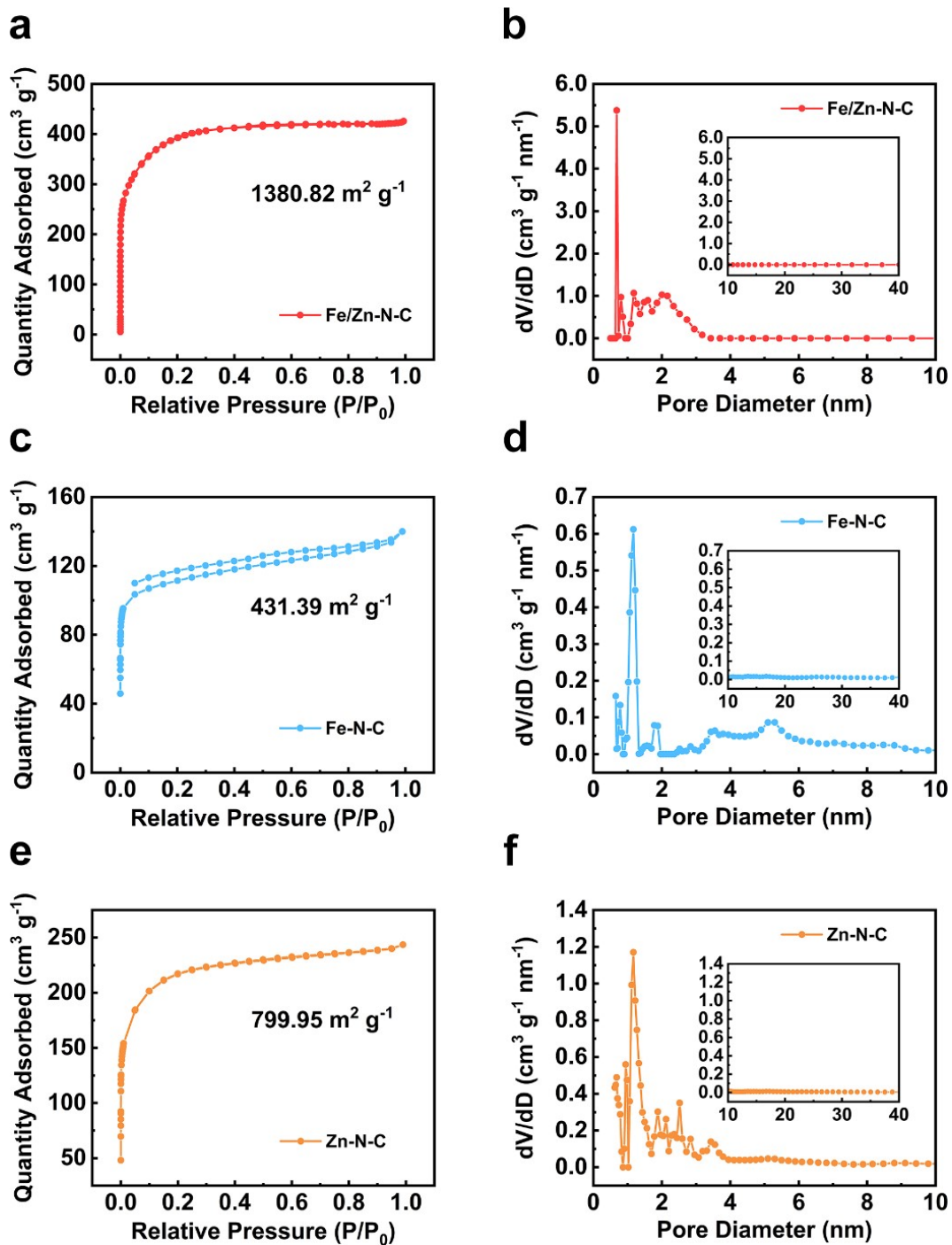
Figure S7. The surface area and pore size distribution information of (a-b) Fe/Zn-N-C, (c-d) Fe-N-C and (e-f) Zn-N-C.
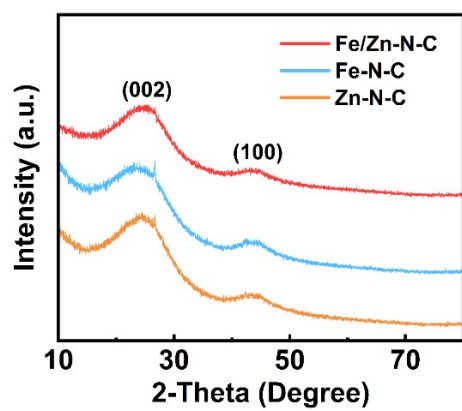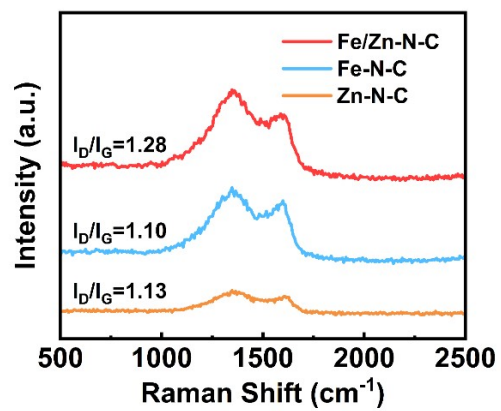
Figure S8. XRD patterns of Fe/Zn-N-C, Fe-N-C and Zn-N-C.

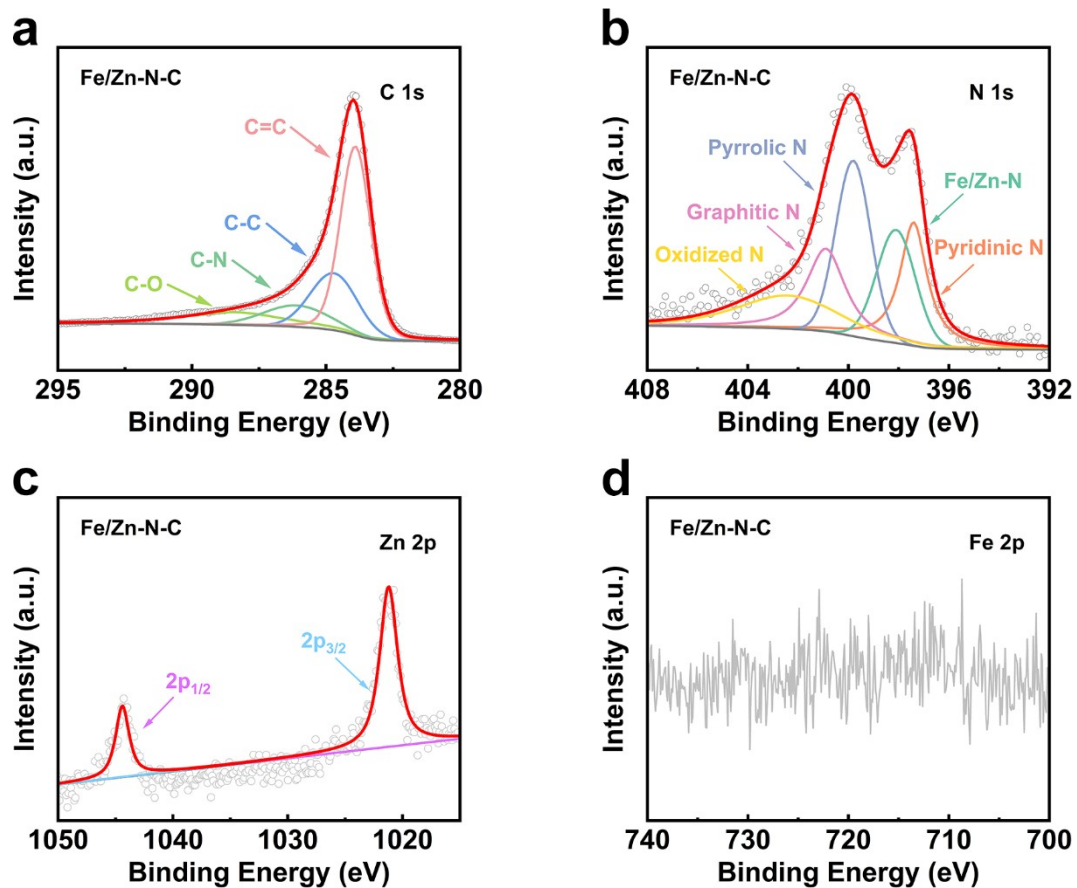**Figure S9.** Raman spectra of Fe/Zn-N-C, Fe-N-C and Zn-N-C.

Figure S10. Fe/Zn-N-C XPS characterization. (a) High-resolution XPS spectra for C 1s. (b) High-resolution XPS spectra for N 1s. (c) High-resolution XPS spectra for Zn 2p. (d) High-resolution XPS spectra for Fe 2p.
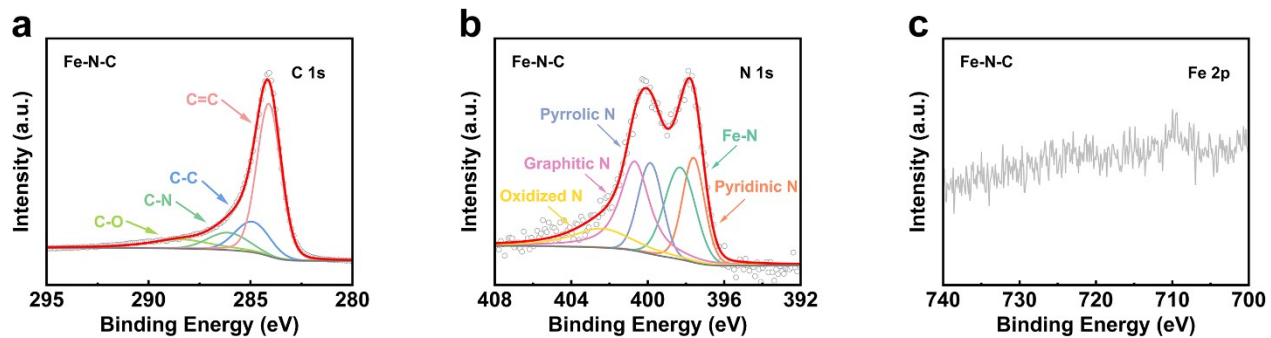
Figure S11. Fe-N-C XPS characterization. (a) High-resolution XPS spectra for C 1s. (b) High-resolution XPS spectra for N 1s. (c) High-resolution XPS spectra for Fe 2p.
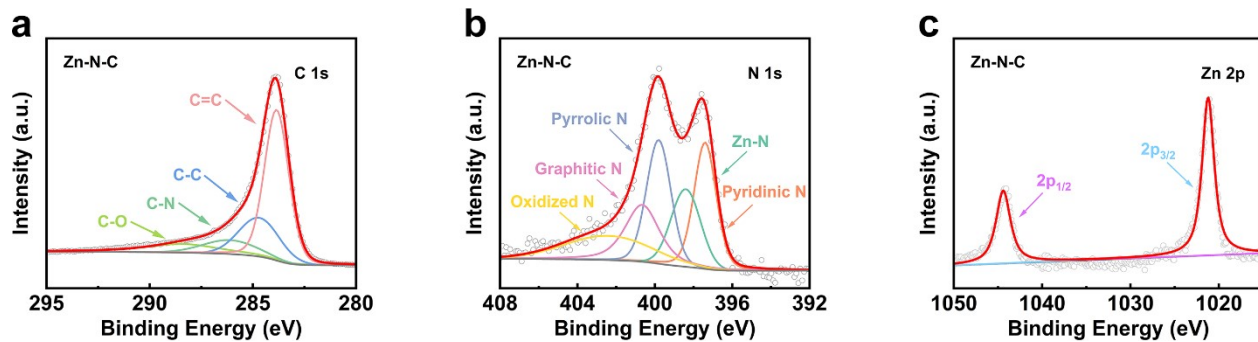
Figure S12. Zn-N-C XPS characterization. (a) High-resolution XPS spectra for C 1s. (b) High-resolution XPS spectra for N 1s. (c) High-resolution XPS spectra for Zn 2p.
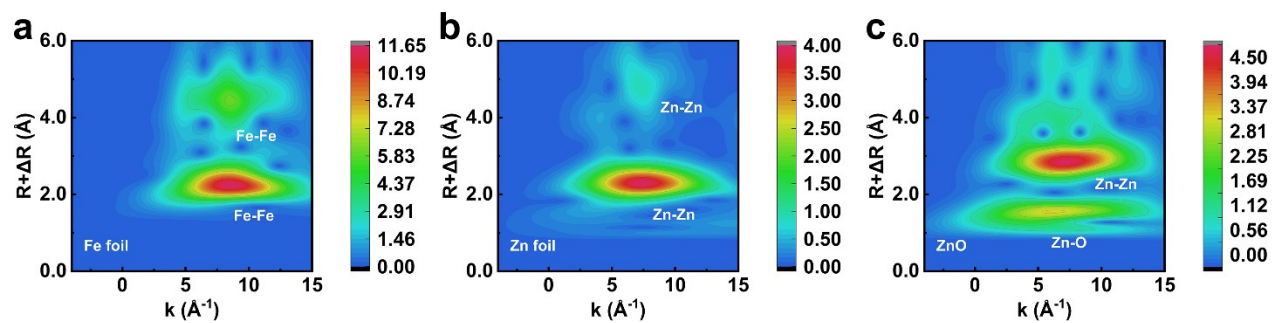
Figure S13. The two possible configurations of FeZnN$_8$

Figure S14. Wavelet transform (WT) contour plots of (a) Fe foil, (b) Zn foil and (c) ZnO.
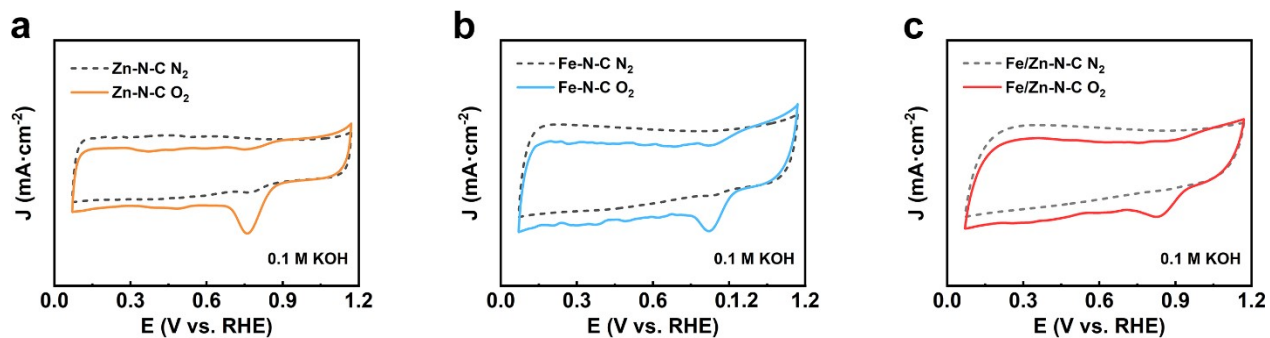
Figure S15. CV curves under N_2-saturated and O_2-saturated 0.1 M KOH solution at a scan rate of 50 mV s^{-1}. (a) Zn-N-C, (b) Fe-N-C and (c) Fe/Zn-N-C.

Figure S16. Fitting the number of transferred electrons. (a) LSV curves at different rotation rates in rpm. (b) Koutecky-Levich plots of Fe-N-C in O_2-saturated 0.1 M KOH solution.

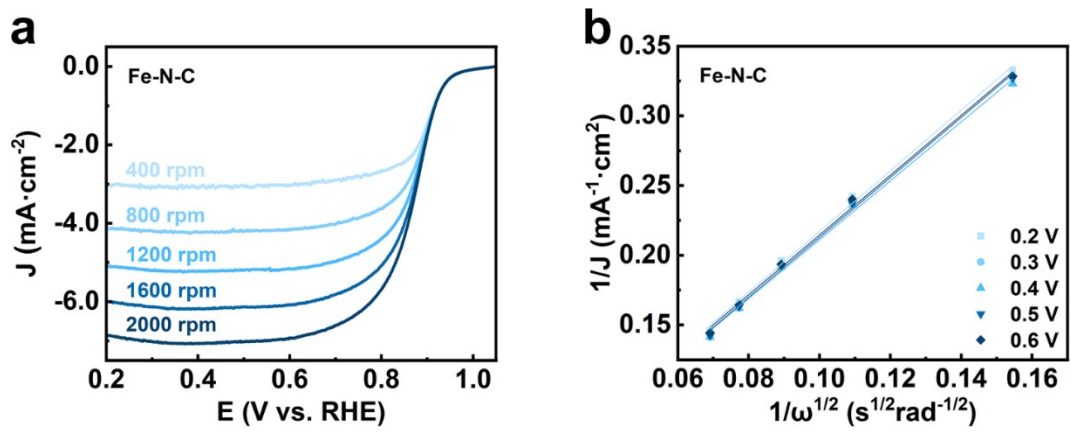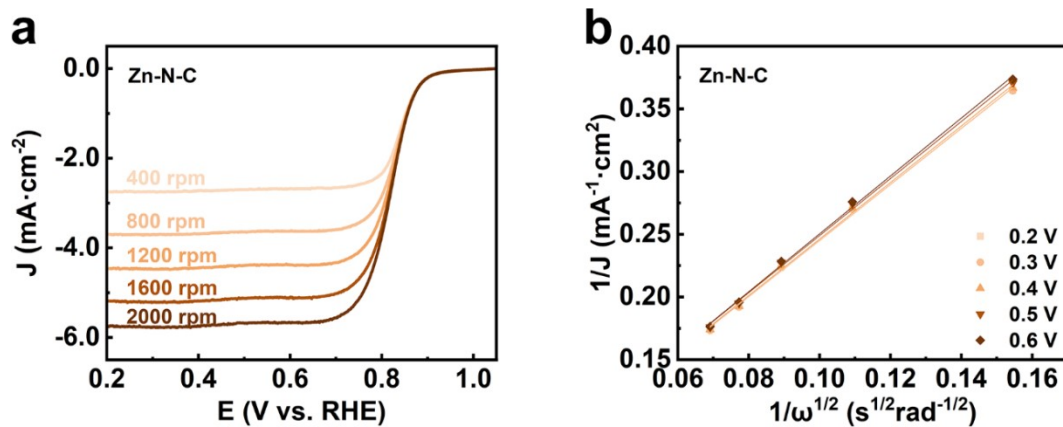**Figure S17.** Fitting the number of transferred electrons. (a) LSV curves at different rotation rates in rpm. (b) Koutecky-Levich plots of Zn-N-C in O_2-saturated 0.1 M KOH solution.

Figure S18. The kinetic current density of the as-synthesized catalysts and Pt/C in O_2-saturated 0.1 M KOH solution.

Figure S19. CV curves from 0.2 to 0.3 V vs RHE in 0.1 M KOH solution at scan rates of 5, 10, 15, 20, 25, 30, 40 and 50 mV s^{-1}, respectively. (a) Zn-N-C, (b) Fe-N-C, (c) Pt/C and (d) Fe/Zn-N-C.
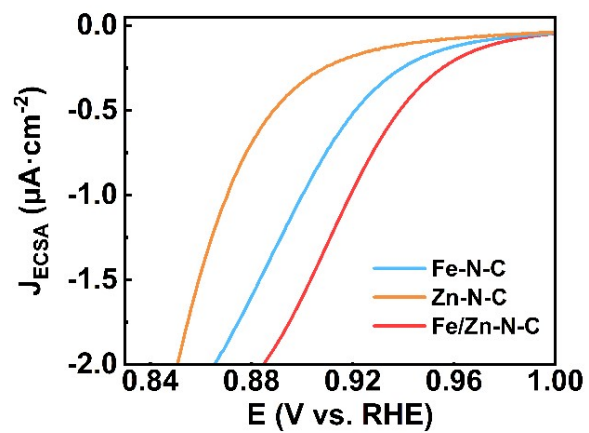
Figure S20. ECSA-normalized LSV curves of Fe-N-C, Zn-N-C and Fe/Zn-N-C in 0.1 M KOH.

Figure S21. Fitting the number of transferred electrons. (a) LSV curves at different rotation rates in rpm. (b) Koutecky-Levich plots of Fe/Zn-N-C in O_2-saturated 0.1 M $HClO_4$ solution.
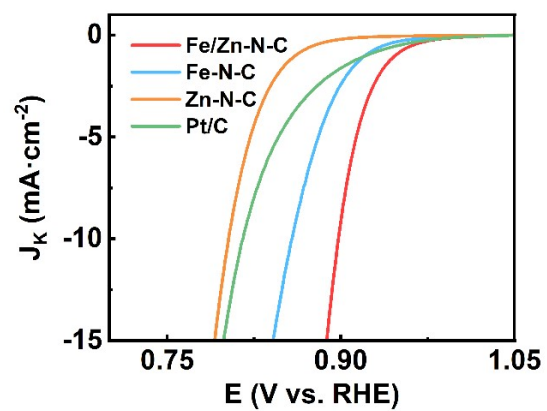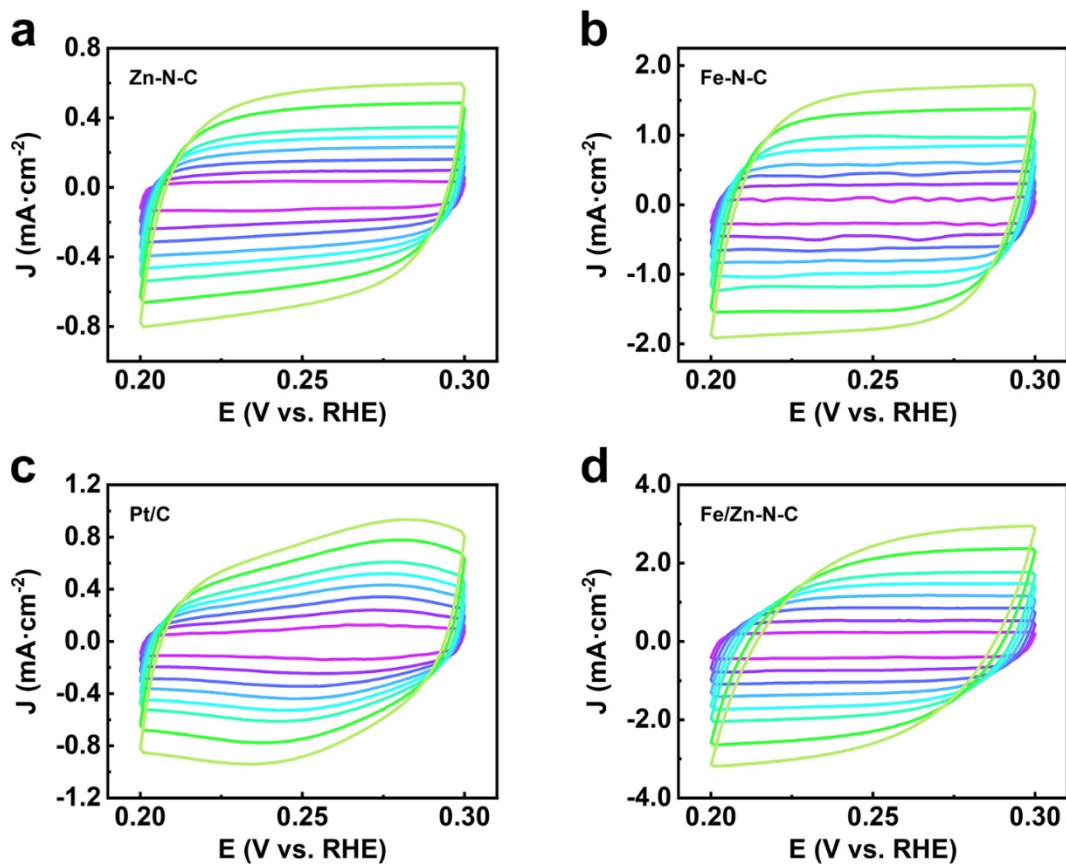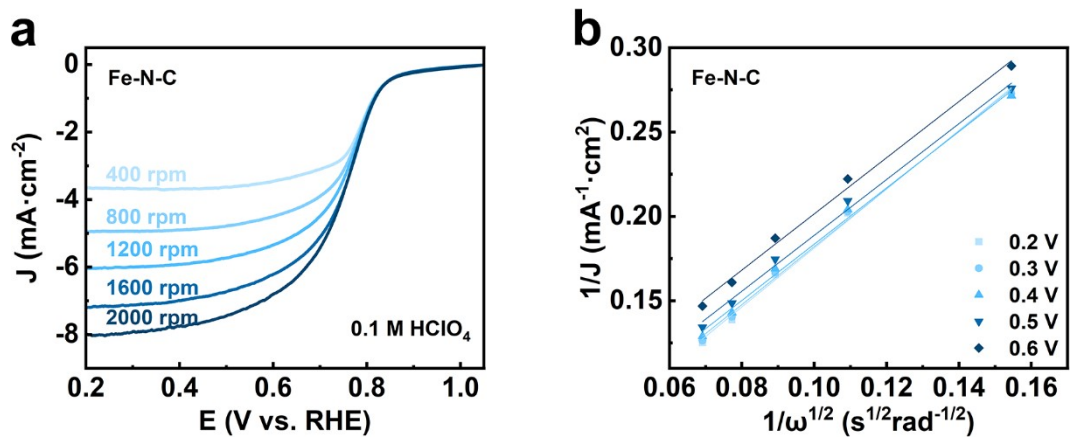
Figure S22. Fitting the number of transferred electrons. (a) LSV curves at different rotation rates in rpm. (b) Koutecky-Levich plots of Fe-N-C in O_2-saturated 0.1 M $HClO_4$ solution.

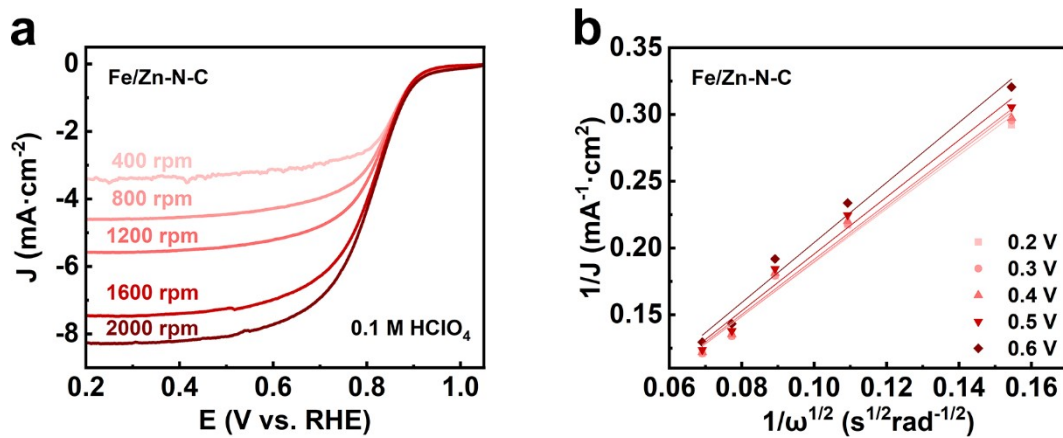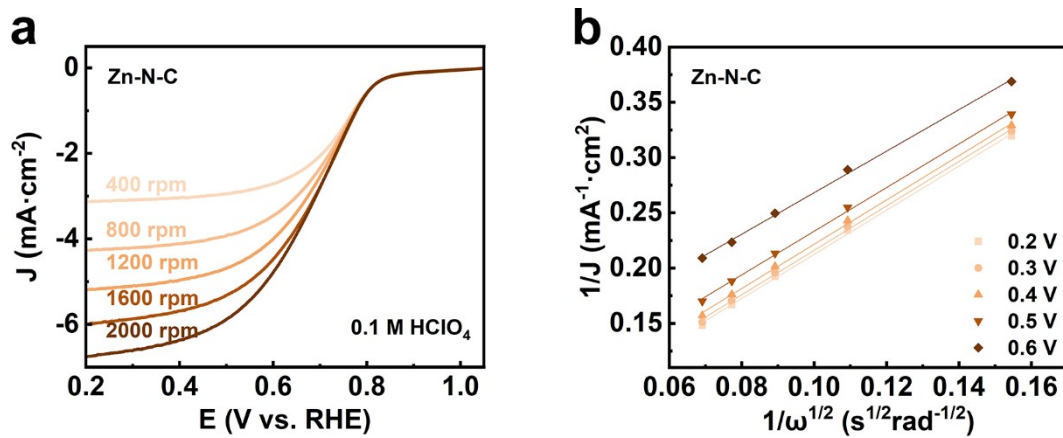**Figure S23.** Fitting the number of transferred electrons. (a) LSV curves at different rotation rates in rpm. (b) Koutecky-Levich plots of Zn-N-C in O_2-saturated 0.1 M $HClO_4$ solution.
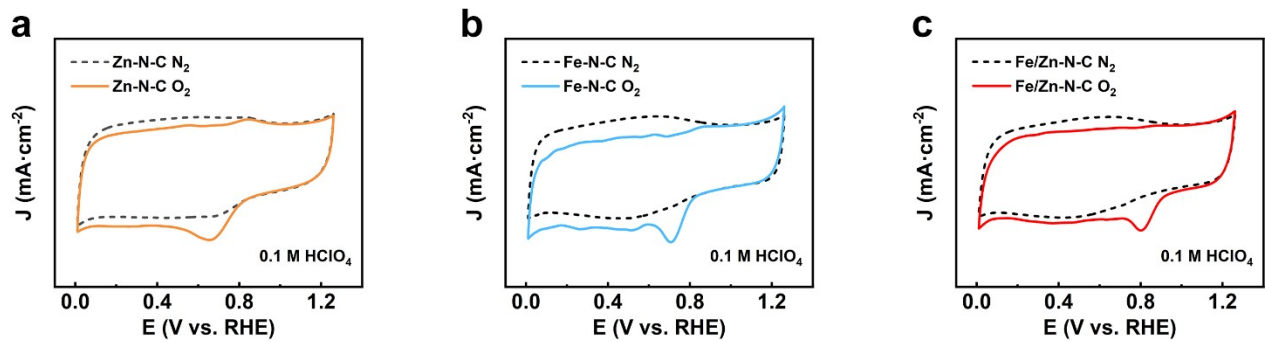
Figure S24. CV curves in N_2- and O_2-saturated 0.1 M $HClO_4$ solution at a scan rate of 50 mV s^{-1}. (a) Zn-N-C, (b) Fe-N-C and (c) Fe/Zn-N-C.
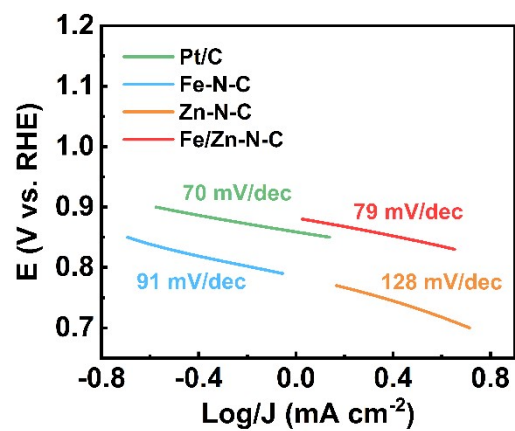
Figure S25. The corresponding Tafel plots obtained from the RRDE polarization curves for ORR in O_2-saturated 0.1 M $HClO_4$ solution.
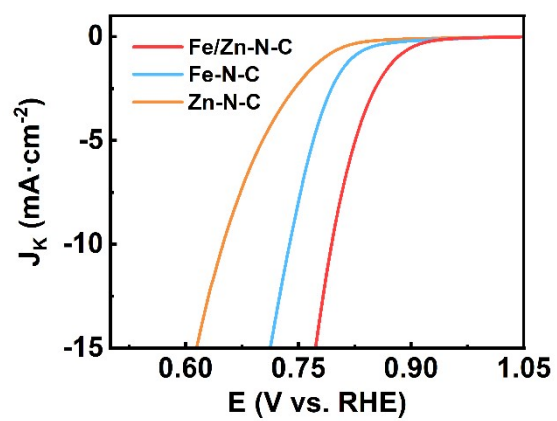
Figure S26. The kinetic current density of the as-synthesized catalysts in O_2-saturated 0.1 M $HClO_4$ solution.
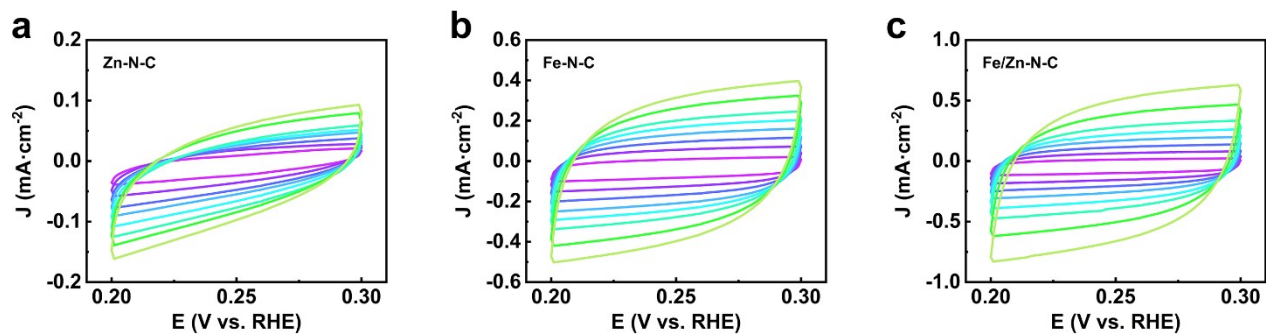
Figure S27. CV curves from 0.2 to 0.3 V vs RHE in 0.1 M HClO$_4$ solution at scan rates of 5, 10, 15, 20, 25, 30, 40 and 50 mV s^{-1}, respectively: (a) Zn-N-C, (b) Fe-N-C and (c) Fe/Zn-N-C.
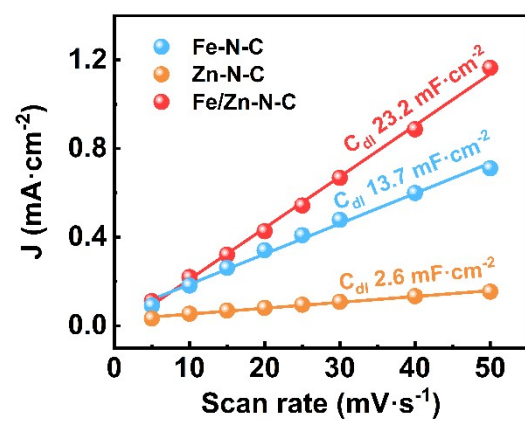
Figure S28. Dependence of current densities as a function of scan rates at 0.25 V vs RHE.
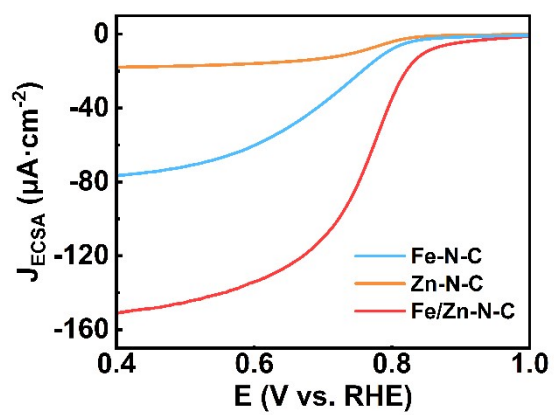
Figure S29. ECSA-normalized LSV curves of Fe-N-C, Zn-N-C and Fe/Zn-N-C in 0.1 M HClO$_4$.
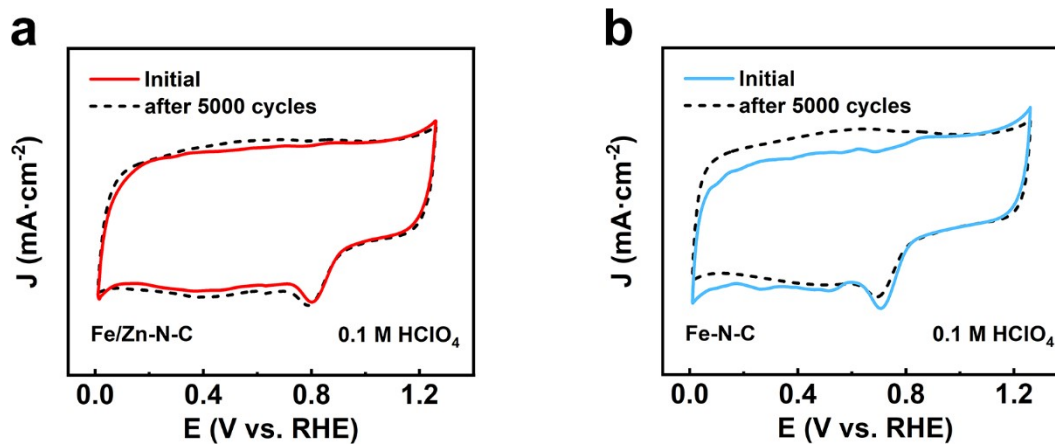
Figure S30. CV curves measured before and after 5000 potential cycles at the scan rate of 50 mV s^{-1} in 0.1 M HClO$_4$ solution. (a) Fe/Zn-N-C and (b) Fe-N-C.
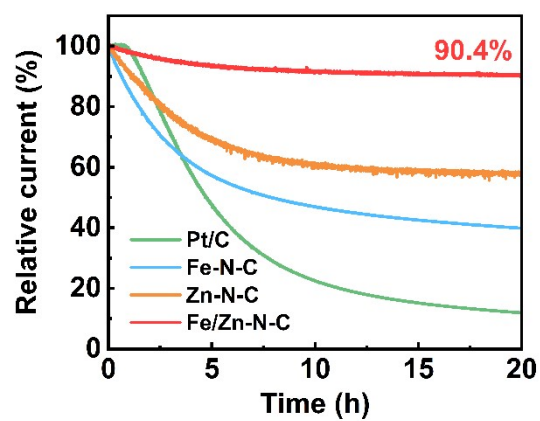
Figure S31. The chronoamperometric response of Pt/C, Fe-N-C, ZnN-C and Fe/Zn-N-C in an O$_2$-saturated 0.1 M HClO$_4$ solution.
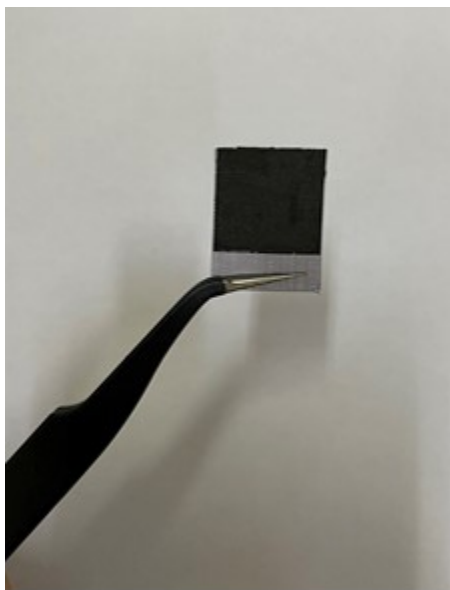
Figure S32. The photograph of catalysts loaded before cycling for ICP-MS measurements on the residual metal amounts in the electrolyte.
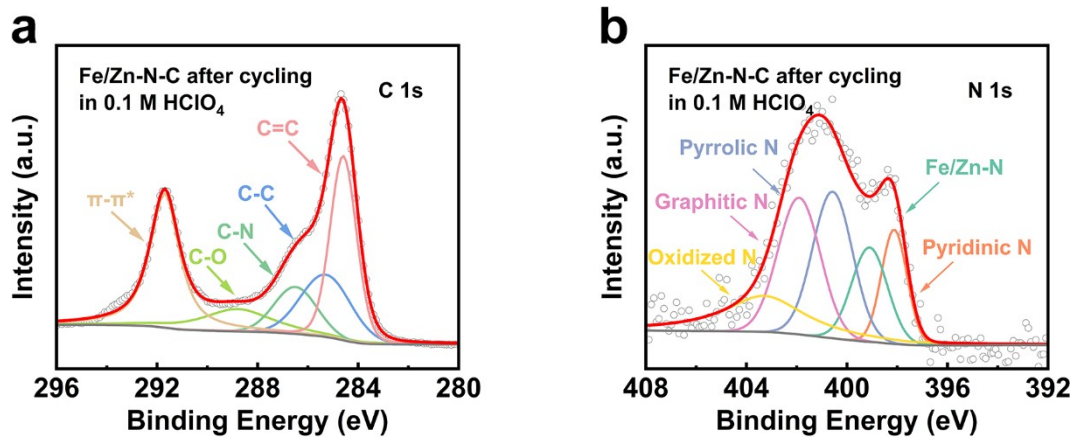
Figure S33. High-resolution XPS spectra of (a) C 1s and (b) N 1s for Fe/Zn-N-C after 5000 cycles.
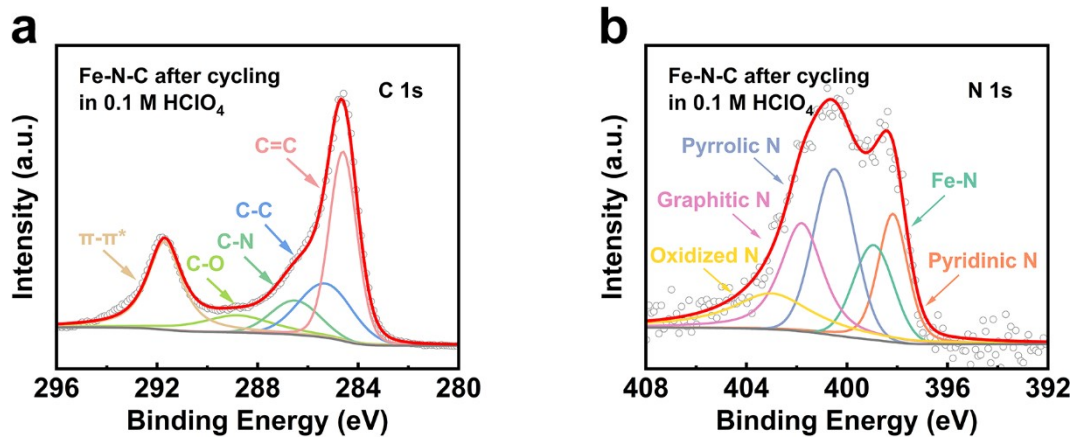
Figure S34. High-resolution XPS spectra of (a) C 1s and (b) N 1s for Fe -N-C after 5000 cycles.
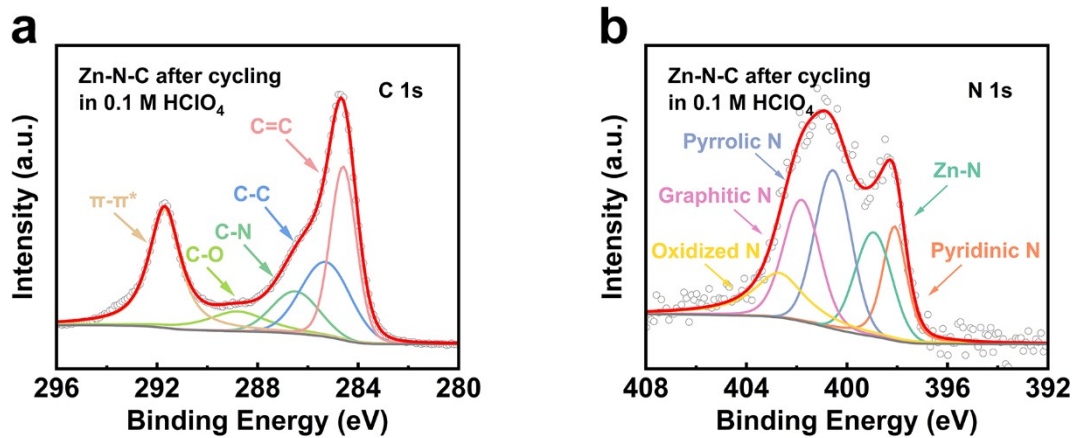
Figure S35. High-resolution XPS spectra of (a) C 1s and (b) N 1s for Zn-N-C after 5000 cycles.
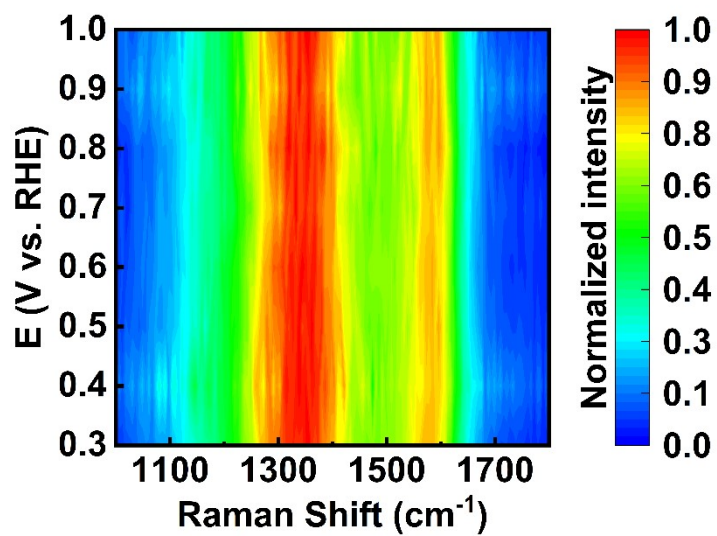
Figure S36. In-situ Raman spectra of Fe/Zn-N-C recorded at various potentials (from 1.0 to 0.3 V vs RHE) in O_2-saturated 0.1 M $HClO_4$ electrolyte.
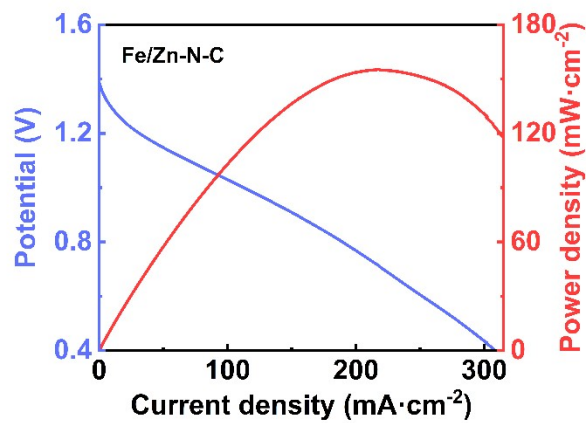
Figure S37. The discharge polarization curve and corresponding power density of the liquid zinc-air battery assembled based on Fe/Zn-N-C.
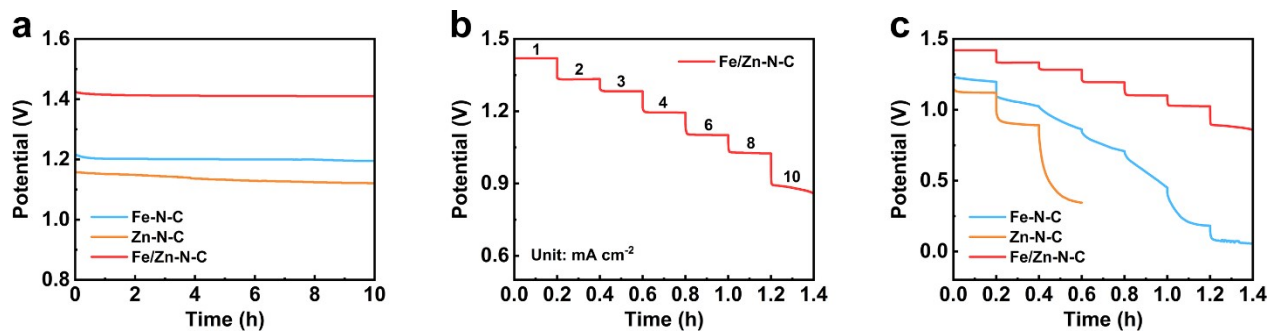
Figure S38. (a) Open circuit voltage of ASS-ZABs based on Fe/Zn-N-C, Fe-N-C and Zn-N-C at the current density of 1 mA cm^{-2}. (b) Discharge curves of Fe/Zn-N-C and (c) the controls (with Fe/Zn-N-C listed as the reference) based ASS-ZABs at different current densities.
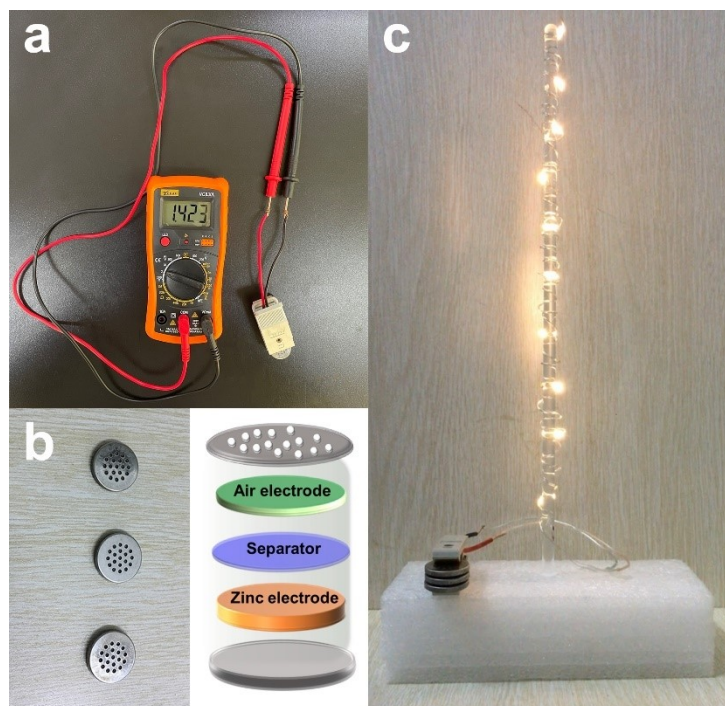
Figure S39. (a) The photograph with an open-circuit voltage of 1.423 V of Fe/Zn-N-C based ASS-ZAB. (b) Photograph and structure diagram of ASS-ZAB. (c) Photograph of light-emitting diodes powered by three Fe/Zn-N-C based ASS-ZABs in series.
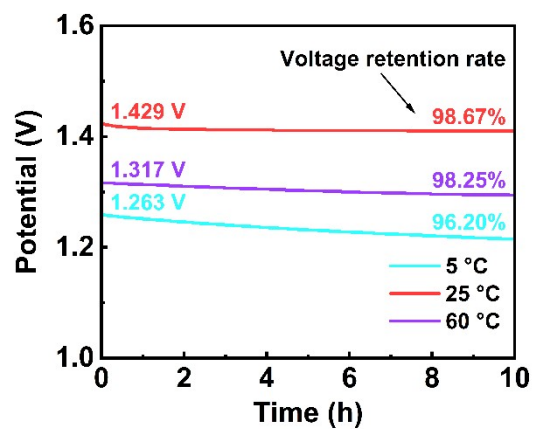
Figure S40. Open circuit voltage of ASS-ZABs based on Fe/Zn-N-C under different temperatures (the current density is 1 mA cm^{-2}).
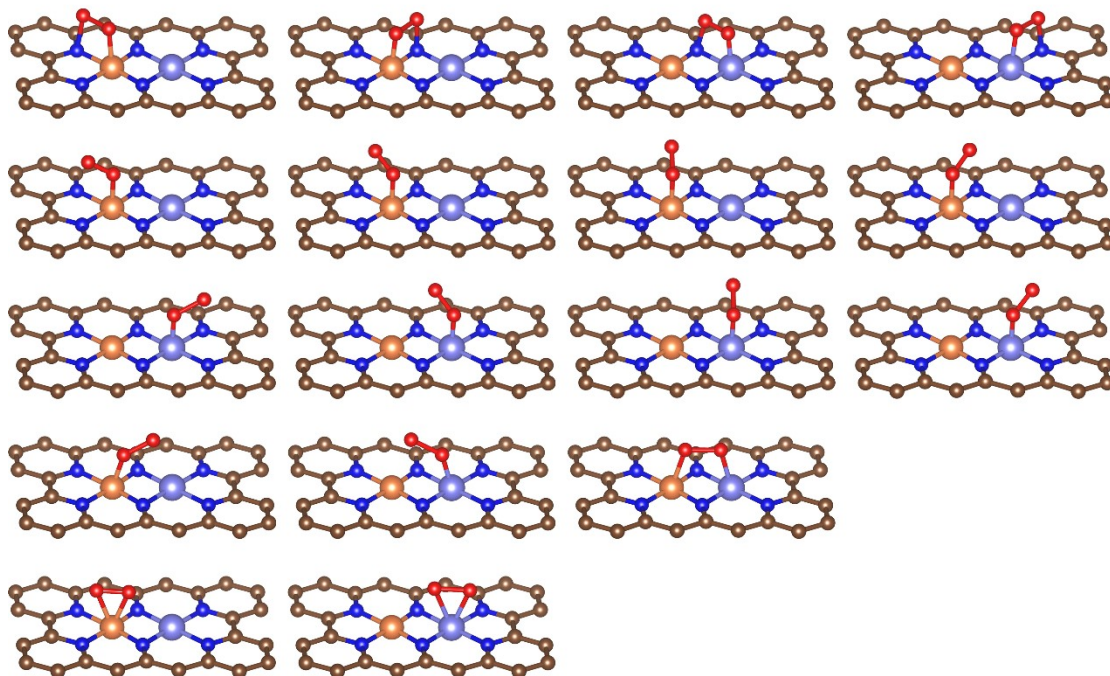
Figure S41. The initial configurations of $*O_2$ for $FeZnN_6$.
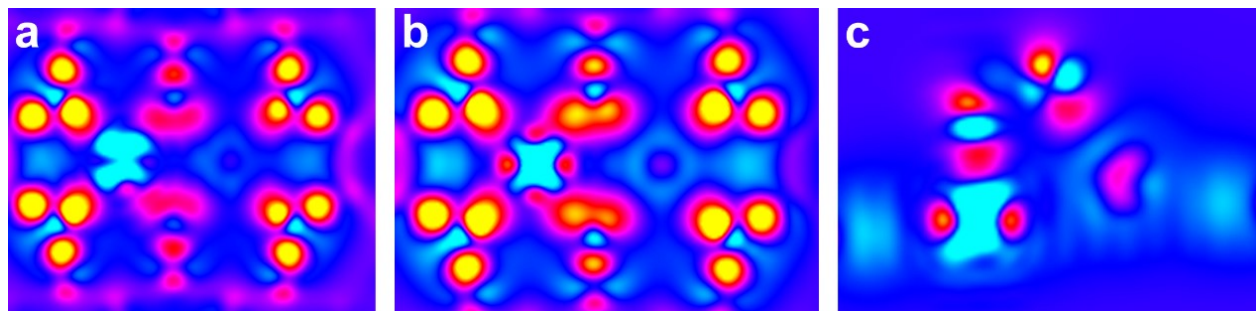
Figure S42. Corresponding two-dimensional projection of charge density contour. (a) Fe/Zn-N-C, (b) Fe/Zn-N-C(OH) and (c) Fe/Zn-N-C(O$_2$).
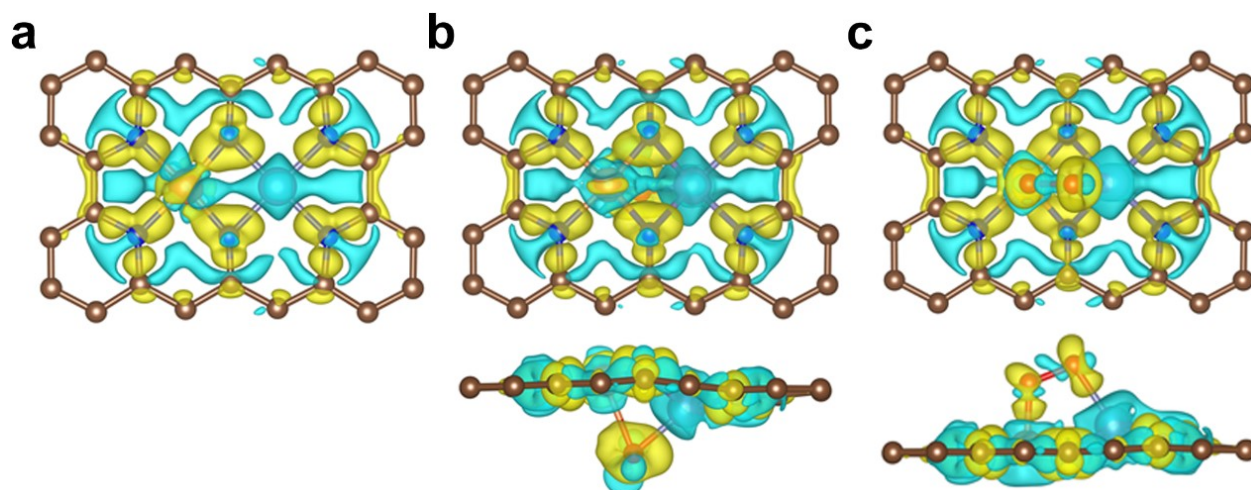
Figure S43. Charge density differences. (a) Fe/Zn-N-C, (b) Fe/Zn-N-C(OH) and (c) Fe/Zn-N-C(O_2).
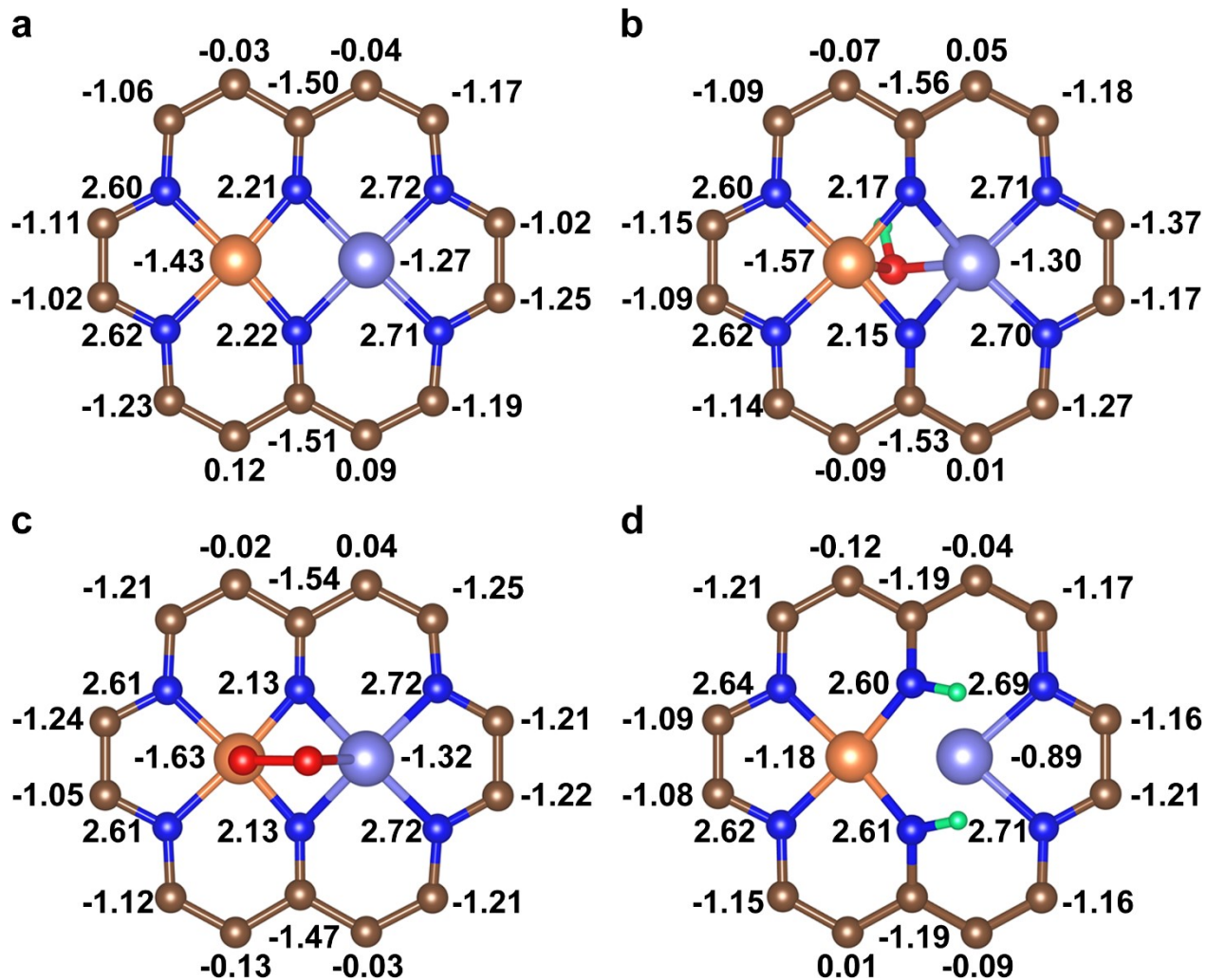
Figure S44. Bader charge. (a) Fe/Zn-N-C, (b) Fe/Zn-N-C(OH), (c) Fe/Zn-N-C(O$_2$) and (d) Fe/Zn-N-C(2*H).
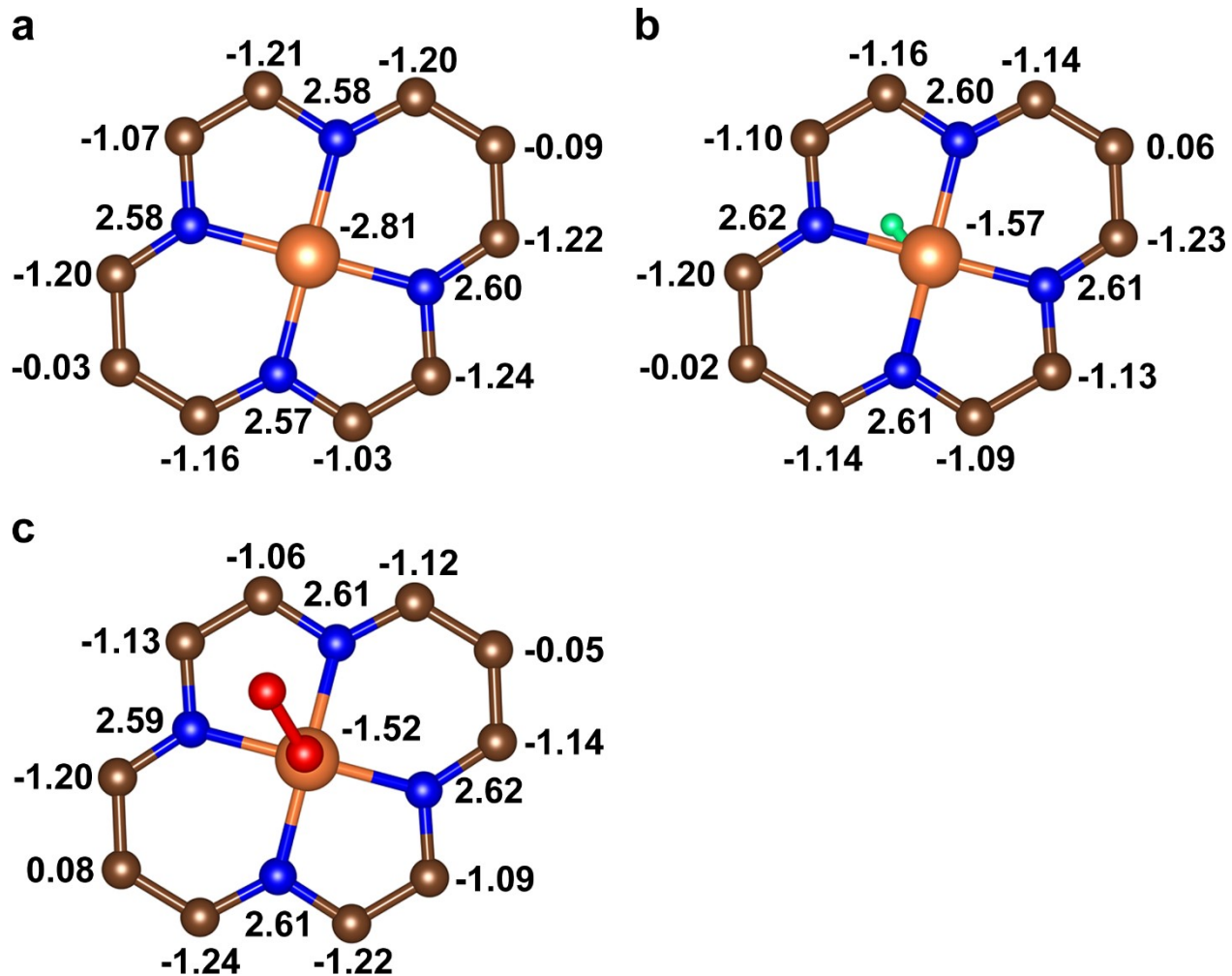
Figure S45. Bader charge. (a) Fe-N-C, (b) Fe-N-C(OH) and (c) Fe-N-C(O_2).
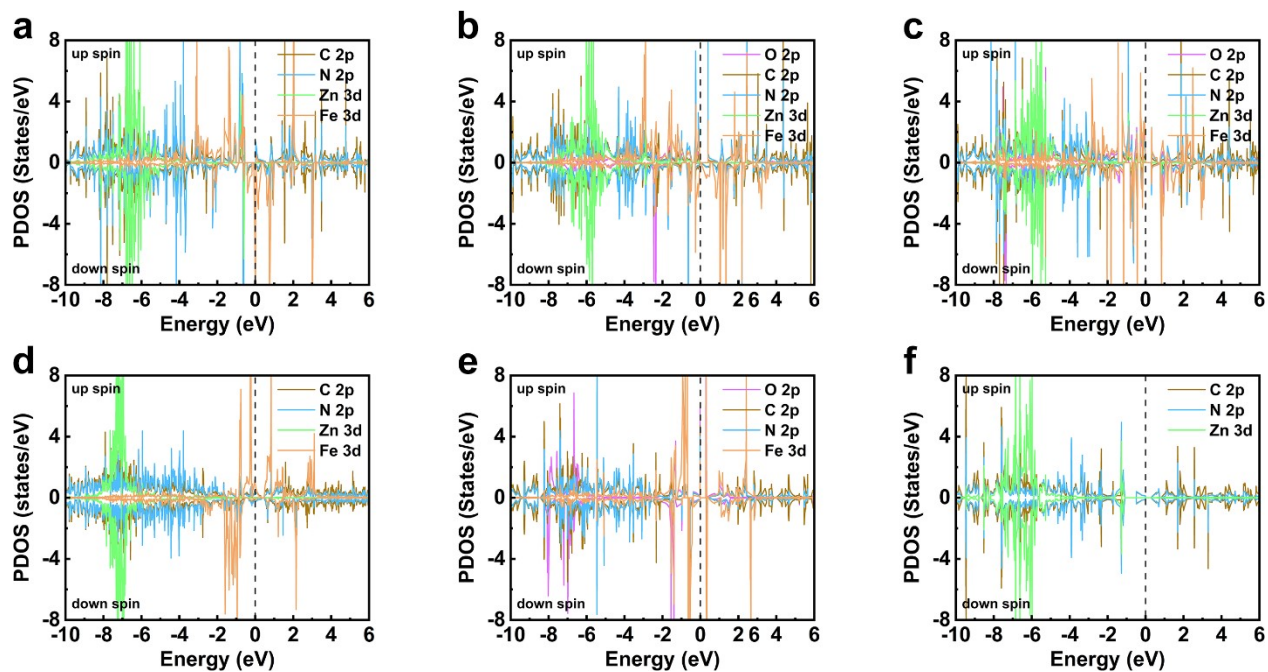
Figure S46. The density of states (DOS) for Fe/Zn 3d and O/C/N 2p. (a) Fe/Zn-N-C, (b) Fe/Zn-N-C(OH), (c) Fe/Zn-N-C(O$_2$), (d) Fe/Zn-N-C(2*H), (e) Fe-N-C(O$_2$) and (f) Zn-N-C.
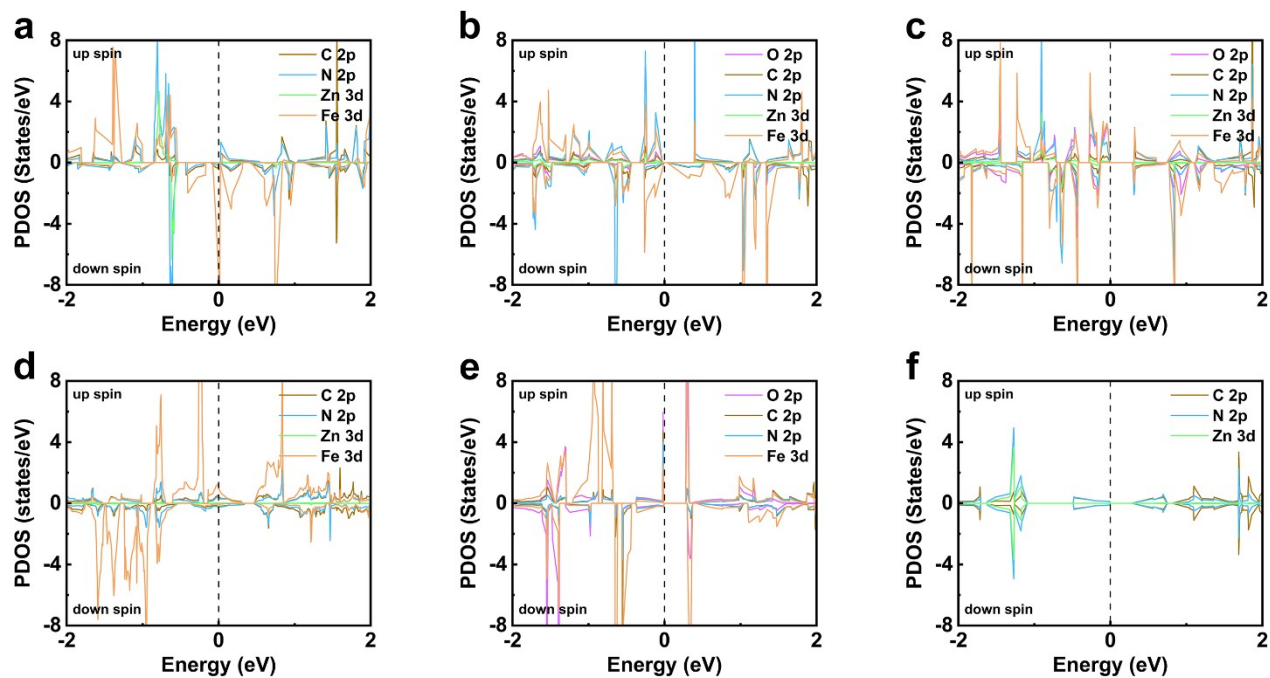
Figure S47. Enlarged DOS of Fe/Zn 3d and O/C/N 2p. (a) Fe/Zn-N-C, (b) Fe/Zn-N-C(OH), (c) Fe/Zn-N-C(O$_2$), (d) Fe/Zn-N-C(2*H), (e) Fe-N-C(O$_2$) and (f) Zn-N-C.
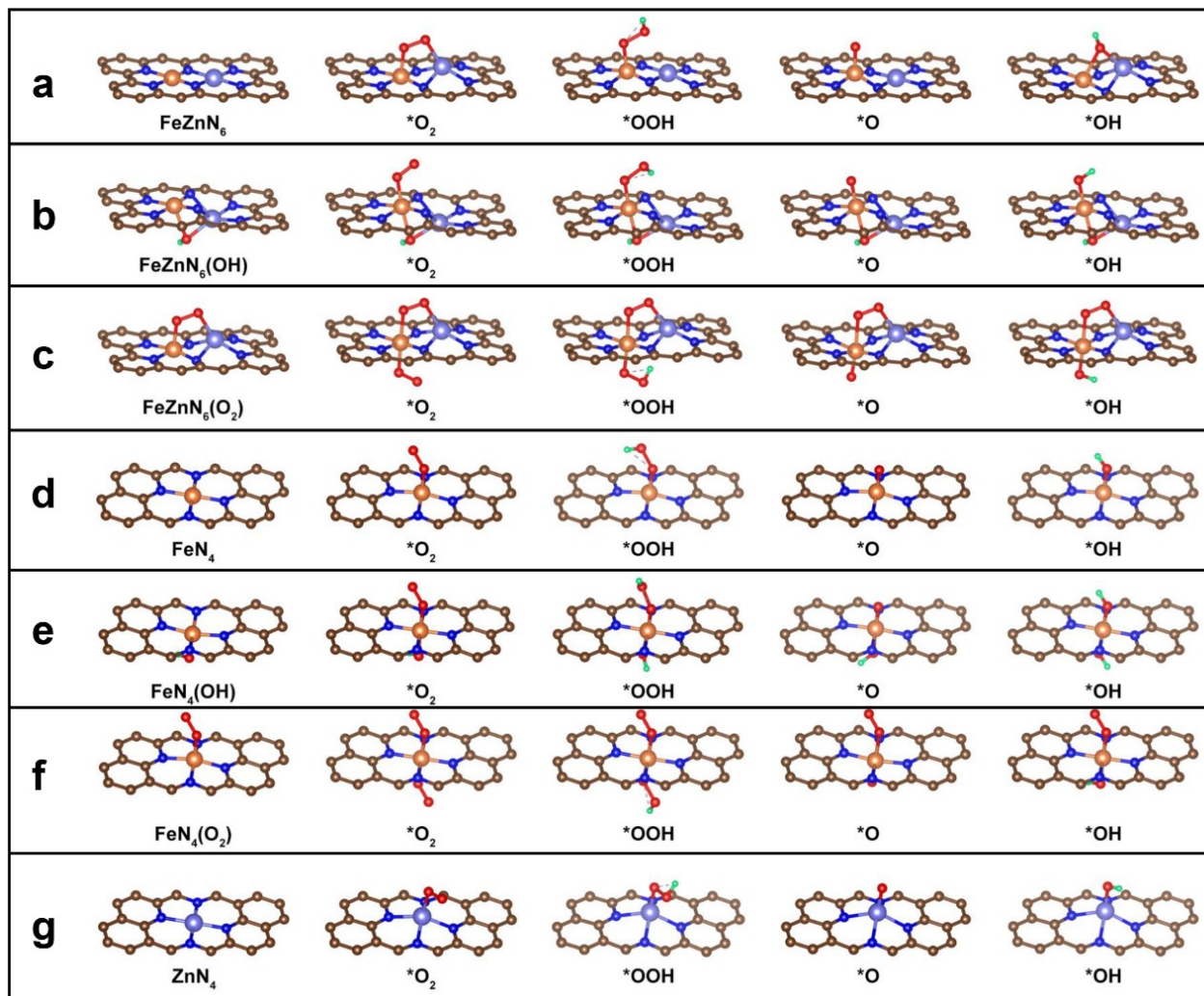
Figure S48. The most stable configurations of key intermediate species (*O_2, *OOH, *O, *OH). (a) Fe/Zn-N-C, (b) Fe/Zn-N-C(OH), (c) Fe/Zn-N-C(O_2), (d) Fe-N-C, (e) Fe-N-C(OH), (f) Fe-N-C(O_2) and (g) Zn-N-C.
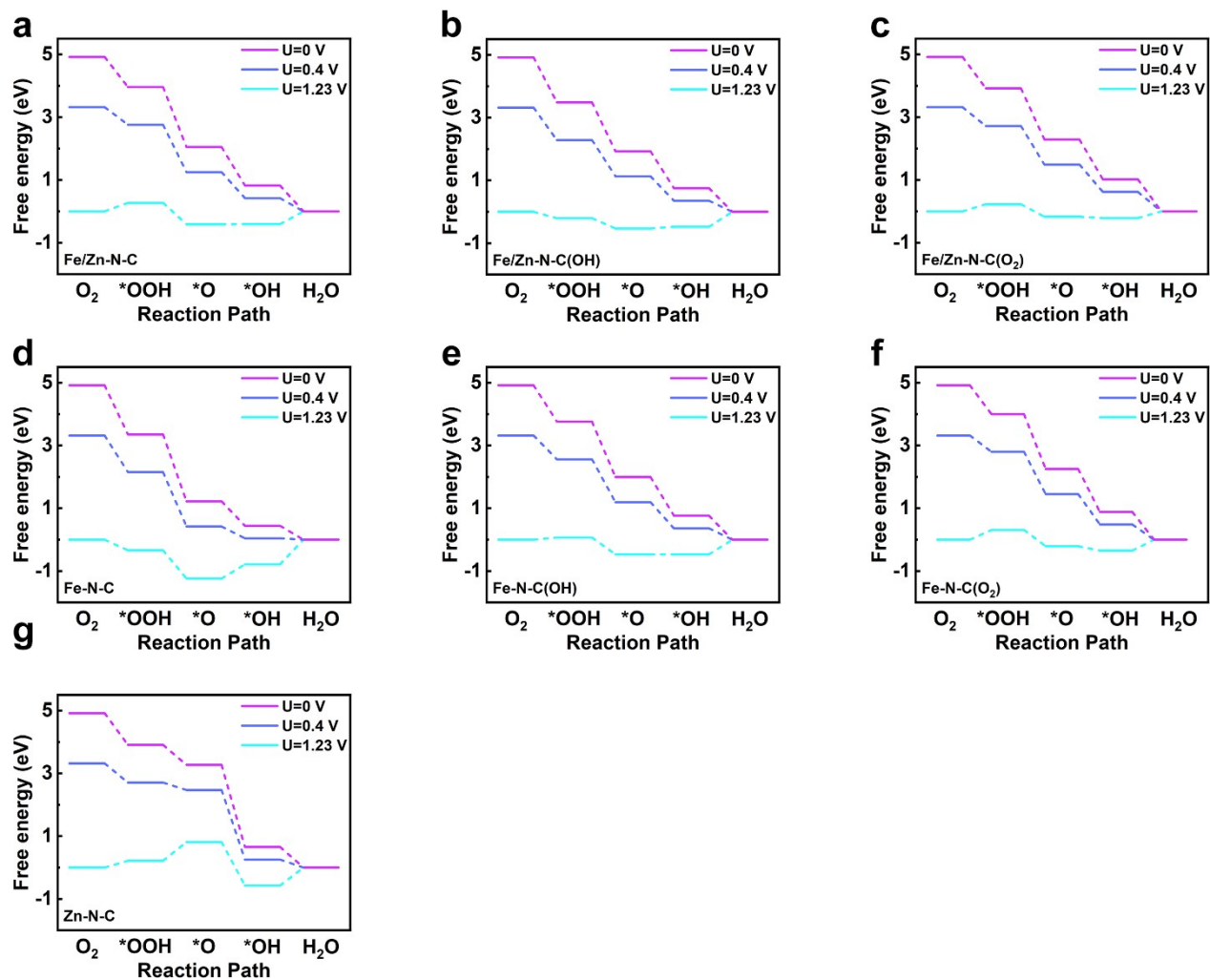
Figure S49. The free energy diagrams at different electrode potentials. (a) Fe/Zn-N-C, (b) Fe/Zn-N-C(OH), (c) Fe/Zn-N-C(O$_2$), (d) Fe-N-C, (e) Fe-N-C(OH), (f) Fe-N-C(O$_2$) and (g) Zn-N-C.
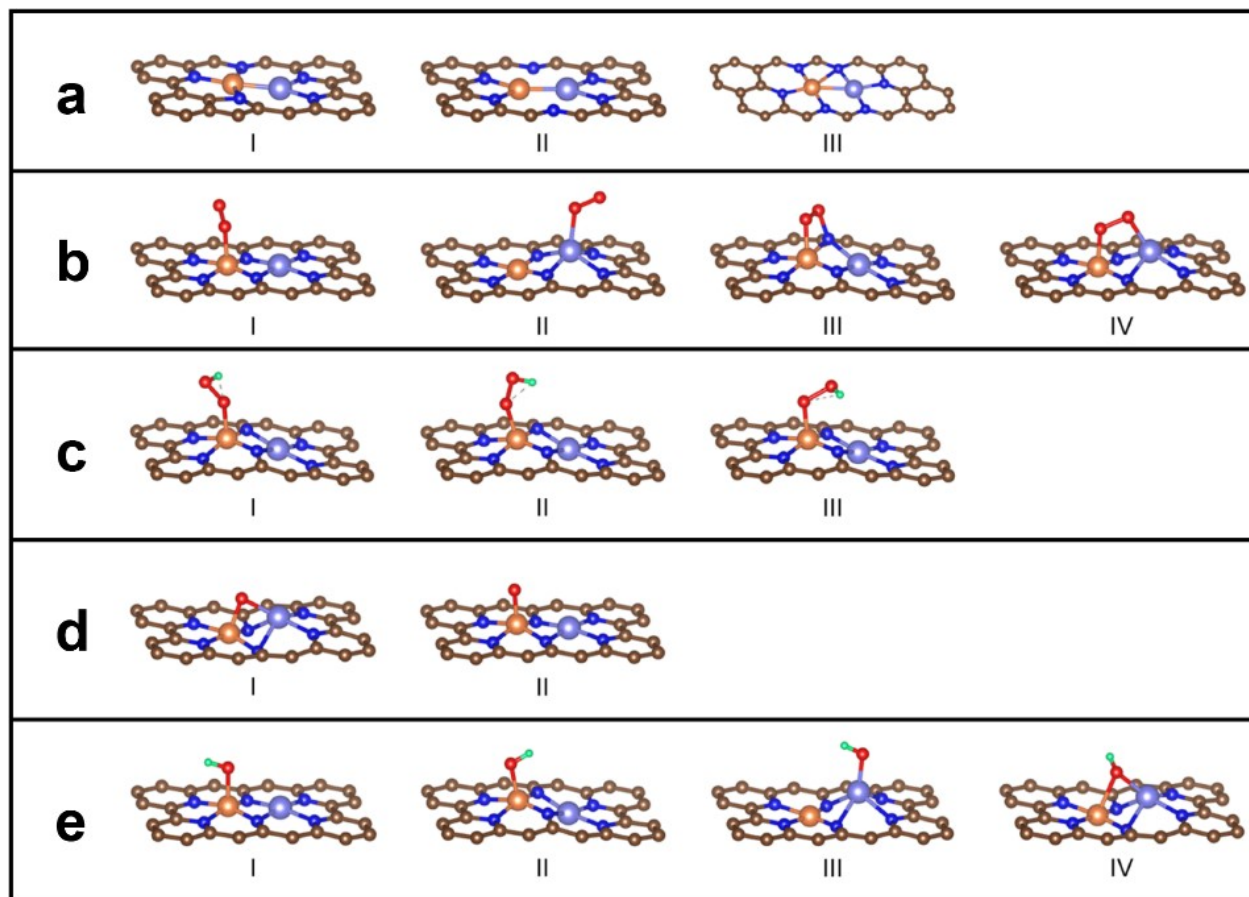
Figure S50. The possible models and all considered configurations of intermediate. (a) Fe/Zn-N-C (b) *O_2, (c) *OOH, (d) *O and (e) *OH.
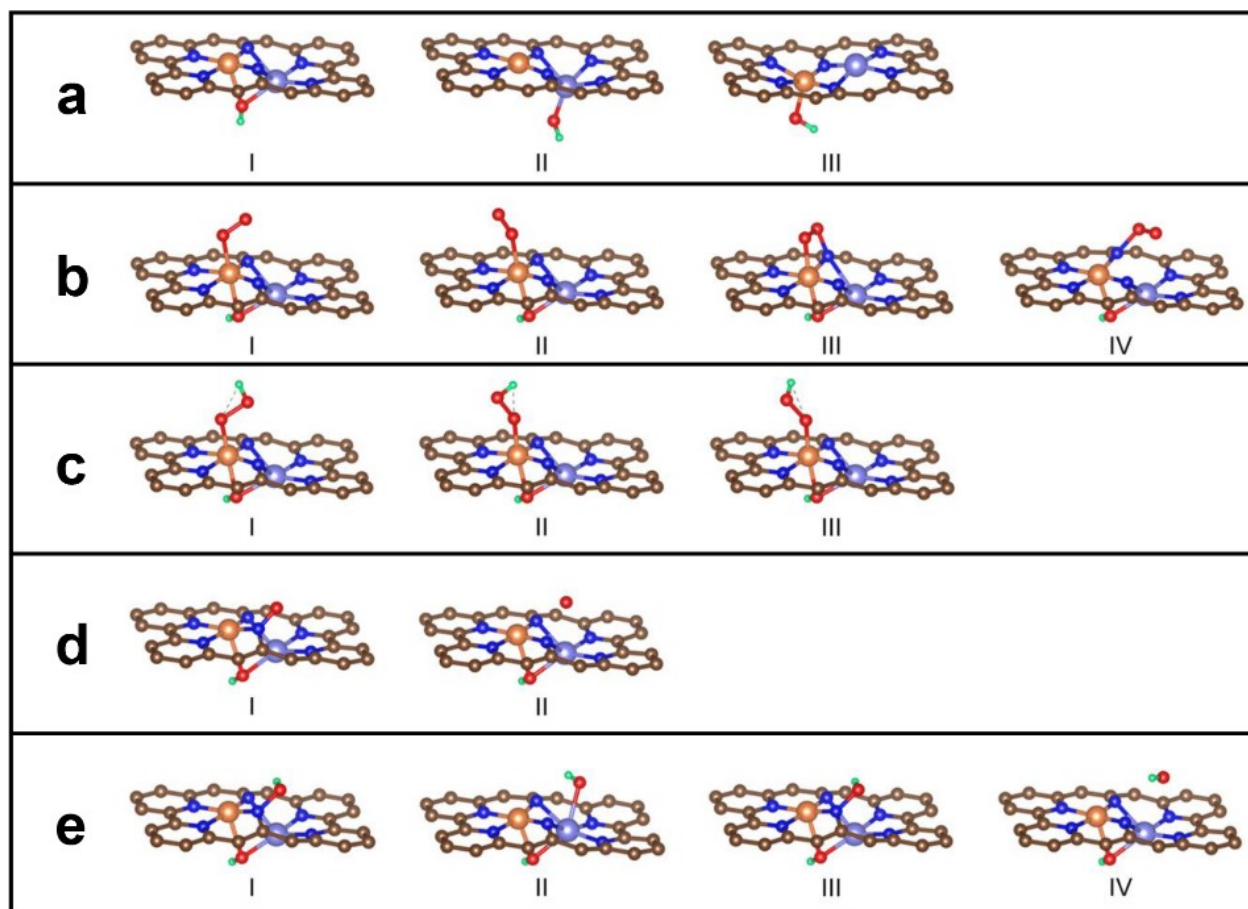
Figure S51. The possible models and all considered configurations of intermediate. (a) Fe/Zn-N-C(OH), (b) $*O_2$, (c) $*OOH$, (d) $*O$ and (e) $*OH$.
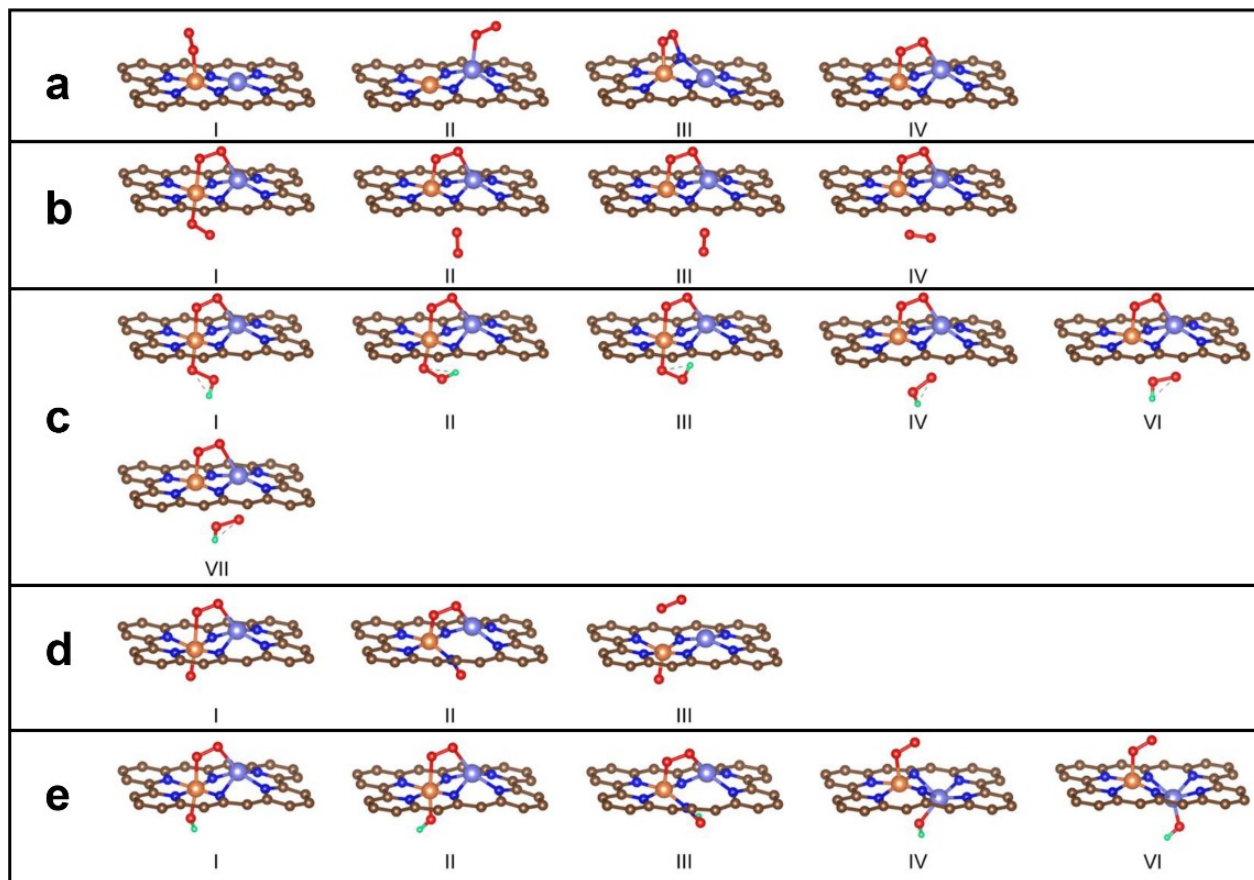
Figure S52. The possible models and all considered configurations of intermediate. (a) Fe/Zn-N-C(O_2), (b) *O_2, (c) *OOH, (d) *O and (e) *OH.
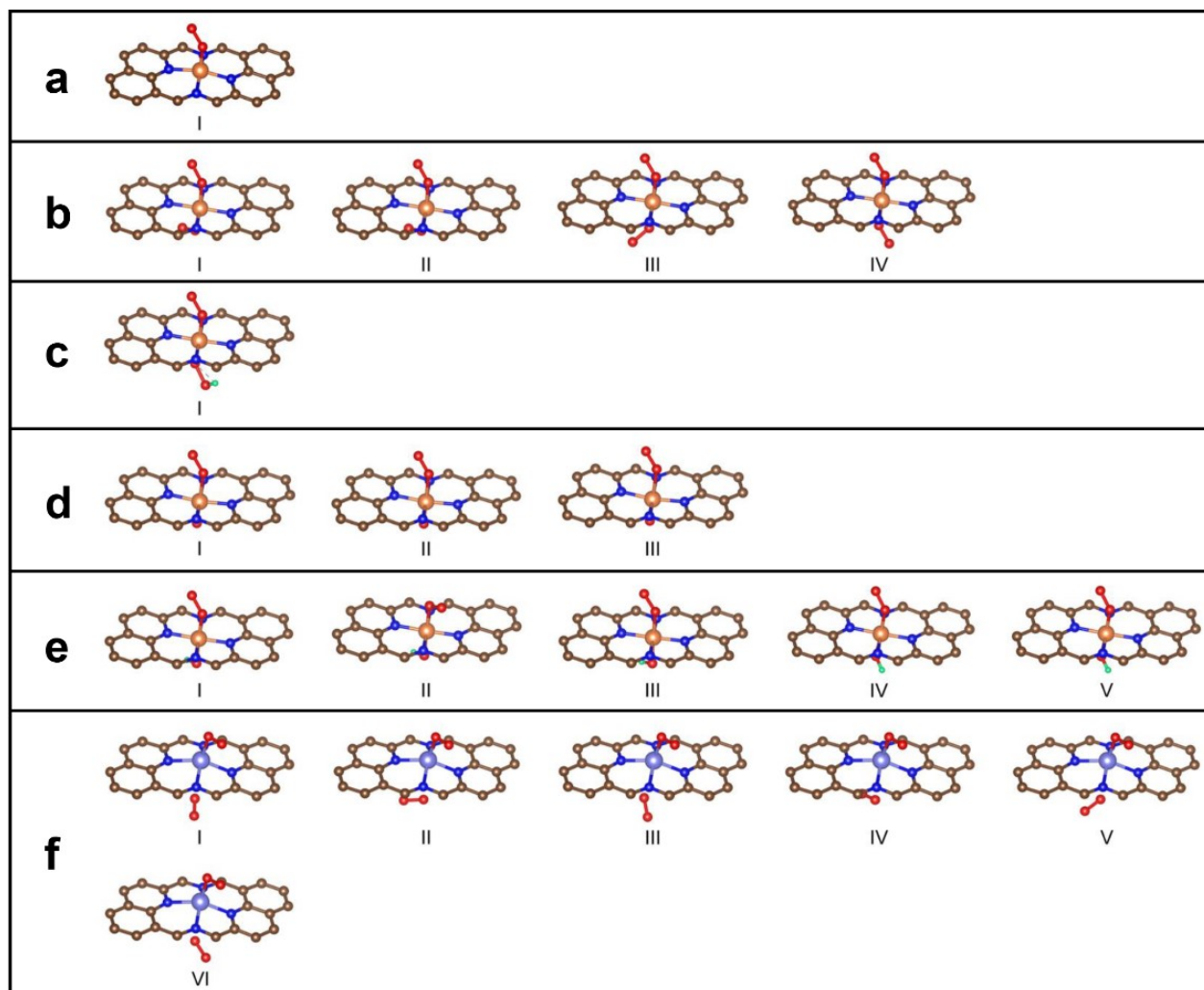
Figure S53. The model and all considered configurations of intermediate. (a) Fe-N-C(O_2), (b) $*O_2$, (c) $*OOH$, (d) $*O$, (e) $*OH$ and (f) $*O_2$.
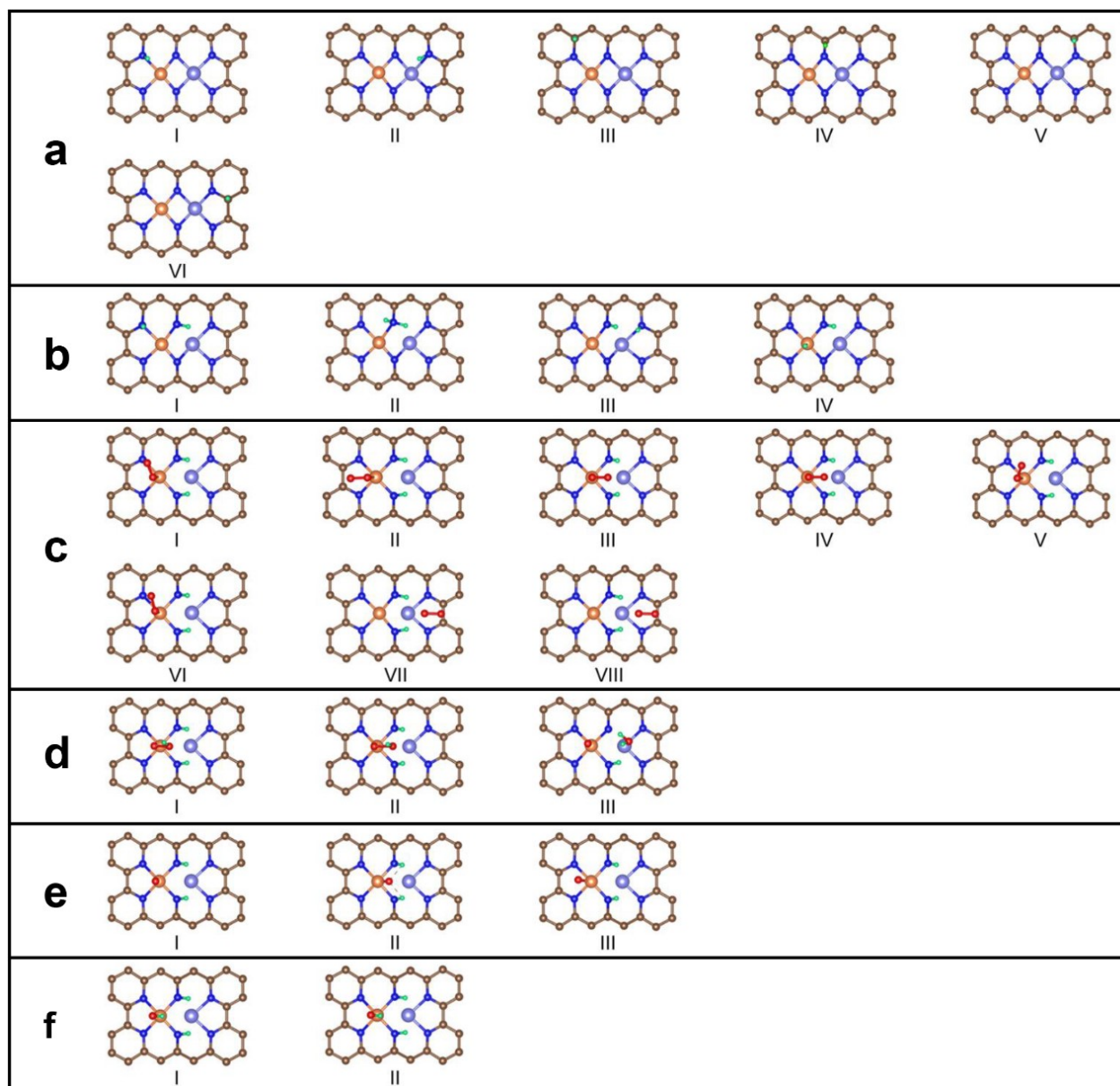
Figure S54. Theoretical simulation of the protonation process. (a) Fe/Zn-N-C(1*H) possible adsorption sites of proton *H. (b) Fe/Zn-N-C(2*H) possible adsorption sites of proton 2*H. All the considered configurations of intermediate (c-f) in the model of Fe/Zn-N-C(2*H): (c) $*O_2$, (d) *OOH, (e) *O and (f) *OH.
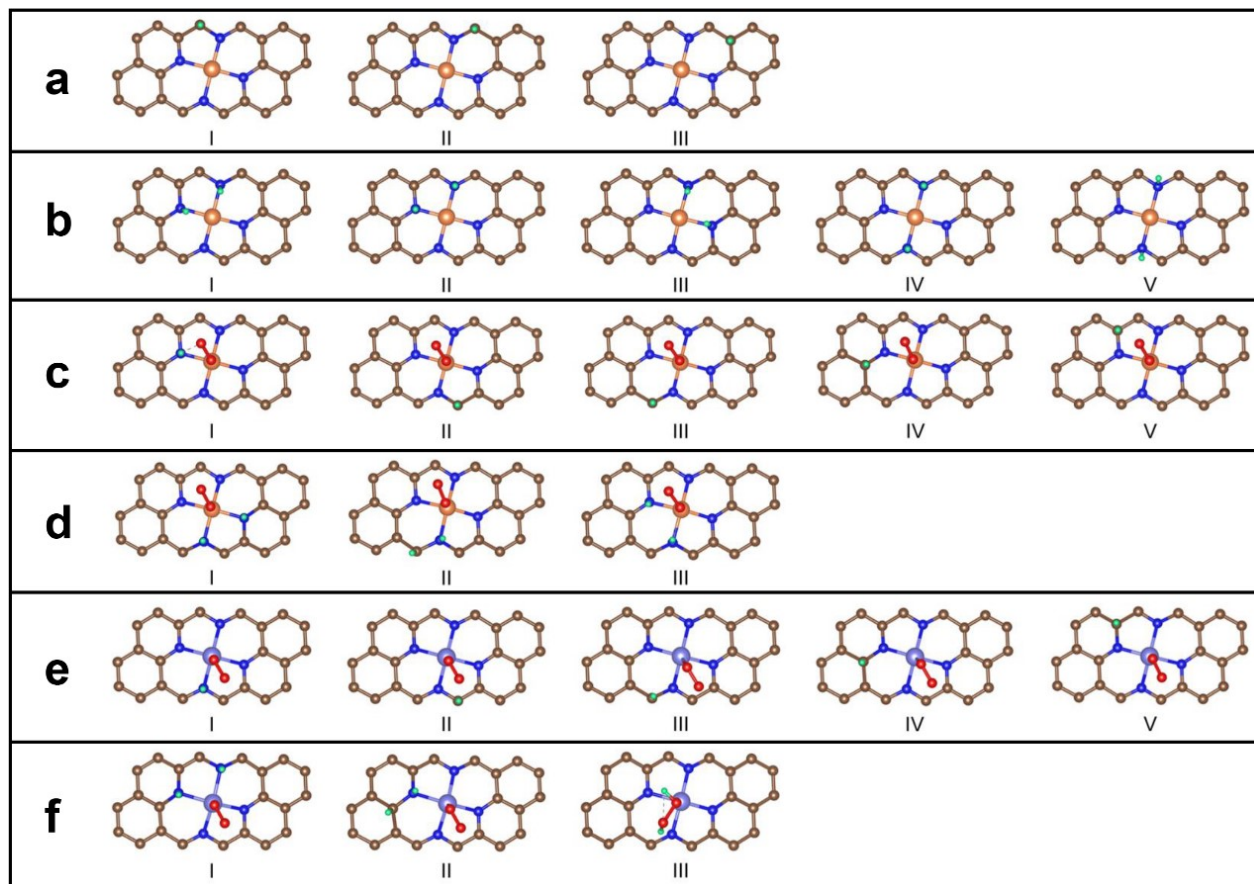
Figure S55. The model of possible adsorption sites of proton *H. (a) Fe-N-C(1*H), (b) Fe-N-C(2*H), (c) Fe-N-C(O_2)(1*H), (d) Fe-N-C(O_2)(2*H), (e) Zn-N-C(1*H) and (f) Zn-N-C(2*H).
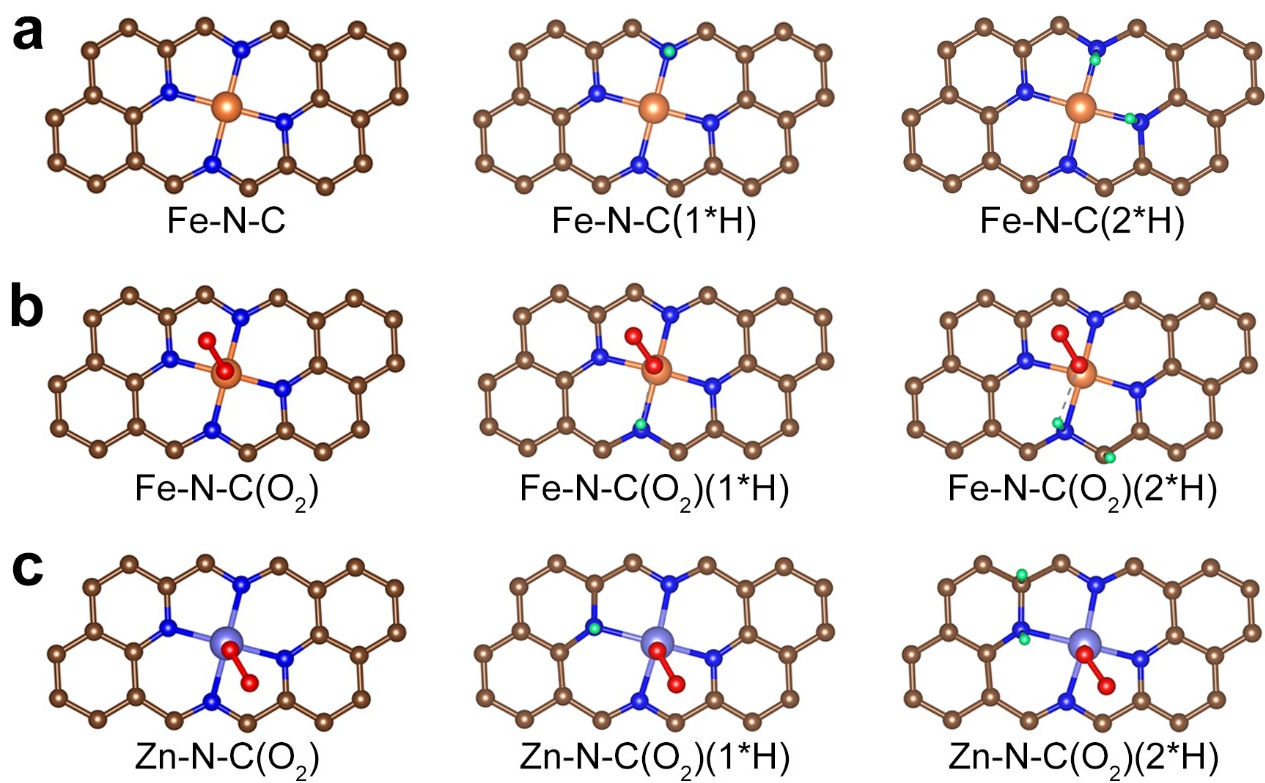
Figure S56. DFT-optimized structures of non-protonated, 1*H protonated, and 2*H protonated species. (a) Fe-N-C, (b) Fe-N-C(O_2) and (c) Zn-N-C(O_2).
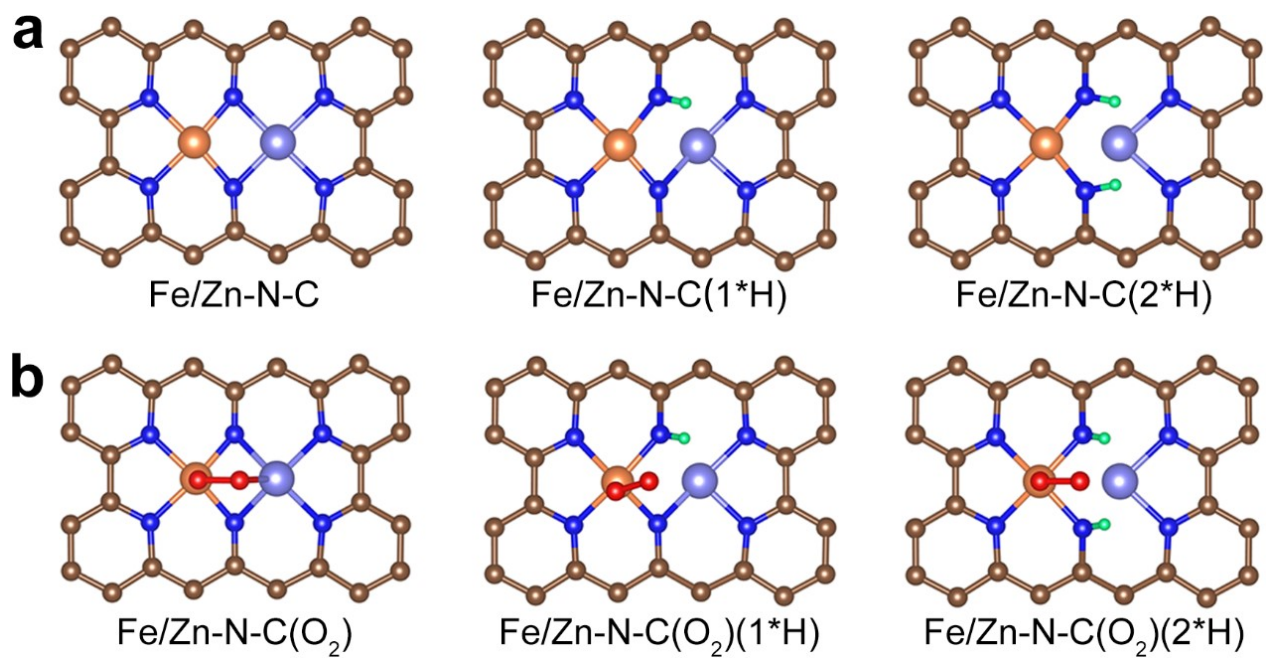
Figure S57. DFT-optimized structures of non-protonated, 1*H protonated, and 2*H protonated species. (a) Fe/Zn-N-C and (b) Fe/Zn-N-C(O_2).

Table S1. The intensity ratio of D and G peaks in the Raman spectra of different samples.

	Fe/Zn-N-C	Fe-N-C	Zn-N-C
I_D/I_G	1.28	1.10	1.13

Table S2. Chemical composition of the Fe/Zn-N-C recorded by XPS.

Elements	Assignment	Position (eV)	Content (at. %)
C	C=C	283.90	51.0
	C-C	284.70	22.4
	C-N	286.09	11.7
	C=O	288.40	14.9
N	Pyridinic N	397.40	20.3
	Fe/Zn-N	398.10	18.4
	Pyrrolic N	399.80	25.4
	Graphitic N	400.89	18.5
	Oxidized N	402.40	17.4
Zn	$2p_{3/2}$	1021.21	74.7
	$2p_{1/2}$	1044.40	25.3

Table S3. Chemical composition of the Fe-N-C recorded by XPS.

Elements	Assignment	Position (eV)	Content (at. %)
C	C=C	284.10	60.7
	C-C	284.90	16.3
	C-N	286.10	10.8
	C=O	288.40	12.2
N	Pyridinic N	397.60	19.4
	Fe-N	398.30	22.3
	Pyrrolic N	399.86	17.4
	Graphitic N	400.68	28.5
	Oxidized N	402.40	12.4

Table S4. Chemical composition of the Zn-N-C recorded by XPS.

Elements	Assignment	Position (eV)	Content (at. %)
C	C=C	283.85	55.1
	C-C	284.70	22.0
	C-N	286.10	10.5
	C=O	288.40	12.4
N	Pyridinic N	397.40	20.5
	Zn-N	398.45	23.3
	Pyrrolic N	399.80	23.6
	Graphitic N	400.65	17.6
	Oxidized N	402.42	15.0
Zn	$2p_{3/2}$	1021.21	74.7
	$2p_{1/2}$	1044.40	25.3

Table S5. EXAFS fitting structure parameters of Fe/Zn-N-C.

	CN	R (Å)	σ^2 (Å^2)	ΔE_0 (eV)	R-factor
Fe-N	4	1.97 (2)	0.007 (4)	−2 (1)	0.025
Zn-N	4	2.01 (4)	0.01 (1)	−1 (3)	0.033

CN is the coordination number; R is interatomic distance (the bond length between central atoms and surrounding coordination atoms); σ^2 is Debye-Waller factor (an indicator of thermal and static disorder in absorber-scatter distances); ΔE_0 is edge-energy shift (the difference between the zero kinetic energy value of the sample and that of the theoretical model). R factor is used to value the goodness of the fitting.

Table S6. Comparison of ORR performances between Fe/Zn-N-C and other reported carbon-based materials in 0.1 M KOH.

Catalysts	$E_{1/2}$ (V)	J_L (mA cm^{-2})	Journal/Year	Reference
Fe/Zn-N-C	0.906	7.02	-	**This work**
Fe SAC/N-C	0.890	5.60	*Adv. Mater.* (2019)	7
Fe-NC SAC	0.900	5.60	*Nat. Commun.* (2019)	8
FeSA-N-C	0.891	6.00	*Angew. Chem. Int. Ed.* (2018)	9
FeNCS	0.882	5.70	*Angew. Chem. Int. Ed.* (2020)	10
HP-FeN$_4$	0.860	5.65	*Energy Environ. Sci.* (2020)	11
Fe1-HNC-500-850	0.85	5.80	*Adv. Mater.* (2020)	12
S,N-Fe/N/C-CNT	0.85	6.68	*Angew. Chem. Int. Ed.* (2017)	13
Fe-SAs/NSC	0.87	6.00	*J. Am. Chem. Soc.* (2019)	14
Zn-N-C	0.873	<5	*Angew. Chem. Int. Ed.* (2019)	15
Cu/Zn-NC	0.83	~5.8	*Angew. Chem. Int. Ed.* (2021)	16
Cu-SAs/N-C	0.895	~5.5	*Nat. Catal.* (2018)	17

Table S7. Comparison of ORR performances between Fe/Zn-N-C and its components in 0.1 M HClO$_4$.

Catalysts	Onset Potential (V)	$E_{1/2}$ (V)	J_L (mA cm^{-2})
Fe/Zn-N-C	0.985	0.808	7.45
Fe-N-C	0.872	0.754	7.21
Zn-N-C	0.822	0.689	5.99

Table S8. Comparison of ORR performances between Fe/Zn-N-C and other reported carbon-based materials in acidic electrolytes.

Catalysts	$E_{1/2}$ (V)	Durability test $\Delta E_{1/2}$ (cycle)	Electrolyte	Journal/Year	Reference
Fe/Zn-N-C	0.808	12 mV (5k)	0.1 M HClO$_4$	-	This work
Fe, Mn/N-C	0.804	18 mV (8k)	0.1 M HClO$_4$	*Nat. Commun.* (2021)	18
Fe-N-C	~0.708	-	0.1 M HClO$_4$	*Nat. Commun.* (2020)	19
Fe/OES	0.72	>10 mV (3k)	0.5 M H$_2$SO$_4$	*Angew. Chem. Int. Ed.* (2020)	20
Fe$_2$-N-C	0.78	20 mV (20k)	0.5 M H$_2$SO$_4$	*Chem* (2019)	21
(CM + PANI)-Fe-C	0.80	-	0.5 M H$_2$SO$_4$	*Science* (2017)	22
20Mn-NC-second	0.80	17 mV (30k)	0.5 M H$_2$SO$_4$	*Nat. Catal.* (2018)	23
Zn-N-C	0.746	19.9 mV (1k)	0.1 M HClO$_4$	*Angew. Chem. Int. Ed.* (2019)	15
Cr/N/C-950	0.773	15 mV (20k)	0.1 M HClO$_4$	*Angew. Chem. Int. Ed.* (2019)	24
SnNC	~0.73	-	0.1 M HClO$_4$	*Nat. Mater.* (2020)	25
Cu-SAs/N-C	~0.73	-	0.1 M HClO$_4$	*Nat. Catal.* (2018)	17
Mg-N-C	0.79	-	0.1 M HClO$_4$	*Nat. Commun.* (2020)	26

Table S9. Metal contents before and after CV cycling.

Sample	Fe (μg/L)	Zn (μg/L)
Electrolyte (HClO$_4$)	0	0
Fe/Zn-N-C (Glassy carbon)	8.8	25.4
Fe-N-C (Titanium mesh)	24685.3	-
Zn-N-C (Titanium mesh)	-	4501.0
Fe/Zn-N-C (Titanium mesh)	976.2	2422.7

Table S10. M-N content before and after CV cycling.

Sample	M-N content (initial)	M-N content (after)	Difference
Fe/Zn-N-C	18.4%	15.2%	3.2%
Fe-N-C	22.3%	15.0%	7.4%
Zn-N-C	23.3%	18.1%	5.2%

Table S11. Bader charge of Fe/Zn-N-C and intermediates.

	Q(FeZnN$_6$)	Q(C-total)	Q(ads)	NC
Basal	12.3883	−11.0461	0	1.3422
*O$_2$	11.8395	−12.5884	1.0497	0.3008
*OOH	11.9968	−12.1459	0.4731	0.324
*O	11.8545	−12.2162	0.714	0.3523
*OH	11.9903	−11.2139	0.6331	1.4095

Table S12. Bader charge of Fe/Zn-N-C(OH) and intermediates.

	Q(FeZnN$_6$)	Q(C-total)	Q(ads)	NC
Basal	12.08	−12.55	0.6347	0.1647
*O$_2$	11.8933	−11.4003	1.0505	1.5435
*OOH	11.9151	−12.9697	0.9819	−0.0727
*O	11.7668	−11.3917	1.2694	1.6445
*OH	11.8274	−12.7012	1.0708	0.197

Table S13. Bader charge of Fe/Zn-N-C(O_2) and intermediates.

	Q(FeZnN$_6$)	Q(C-total)	Q(ads)	NC
Basal	11.9851	−12.537	0.802	0.2501
*O$_2$	11.8395	−12.5884	1.0497	0.3008
*OOH	11.9226	−12.7389	1.0755	0.2163
*O	11.7801	−12.5738	1.2699	0.4762
*OH	11.8438	−12.5991	1.0755	0.3202

Table S14. Bader charge of Fe/Zn-N-C(2*H) and intermediates.

	Q(FeZnN$_6$)	Q(C-total)	Q(ads)	NC
Basal	11.5172	−13.8082	2	0.291
*O$_2$	11.8395	−12.5884	1.0497	0.3008
*OOH	11.585	−13.193	1.4233	0.1847
*O	11.4614	−12.9155	1.2692	0.1849
*OH	11.5245	−13.0655	1.4144	0.1266

Table S15. Bader charge of Fe-N-C and intermediates.

	$Q(FeN_4)$	$Q(C\text{-total})$	$Q(ads)$	NC
Basal	7.5281	−9.3157	0	−1.7876
$*O_2$	7.5892	−9.2489	0.4578	−1.2019
*OOH	7.6401	−9.255	0.4208	−1.1941
*O	7.7645	−9.2283	0.6755	−0.7883
*OH	7.6616	−9.2442	−0.4486	−1.134

Table S16. Bader charge of Fe-N-C(OH) and intermediates.

	Q(FeN$_4$)	Q(C-total)	Q(ads)	NC
Basal	8.8736	−9.1818	0.4966	0.1884
*O$_2$	8.8845	−9.588	1.0473	0.3438
*OOH	8.883	−9.6329	1.0864	0.3365
*O	8.8082	−9.8672	1.3104	0.2514
*OH	8.9073	−9.7966	1.0813	0.192

Table S17. Bader charge of Fe-N-C(O_2) and intermediates.

	Q(FeN$_4$)	Q(C-total)	Q(ads)	NC
Basal	8.9029	−9.1833	0.5095	0.2291
*O$_2$	8.9613	−9.4923	0.9096	0.3786
*OOH	8.906	−9.6122	1.0596	0.3534
*O	8.8545	−9.6376	1.1065	0.3234
*OH	8.9018	−9.4701	1.0494	0.4811

Table S18. Binding energy of *O_2 and *OH with Fe/Zn-N-C and Fe-N-C.

	*O_2 (eV)	*OH (eV)
Fe/Zn-N-C	−1.25679737	−0.50805846
Fe-N-C	−1.22161561	−0.14360607

Table S19. Bond lengths before and after Fe/Zn-N-C(O_2) protonation.

	Fe-N_1	Fe-N_2	Fe-N_3	Fe-N_4	Zn-N_3	Zn-N_4	Zn-N_5	Zn-N_6
Fe/Zn-N-C(O_2)	1.94	1.94	1.79	1.79	2.05	2.05	2.02	2.02
FeZnN$_6$(O_2)(H$_2$)	1.92	1.92	1.91	1.91	break	break	2.00	2.00

Supplementary References

1. C. Zhu, C. Kim, Y. Aoki and H. Habazaki, *Adv. Mater. Interfaces*, 2017, **4**, 1700583.
2. G. Kresse and J. Furthmüller, *Comput. Mater. Sci.*, 1996, **6**, 15-50.
3. G. Kresse and J. Furthmüller, *Phys. Rev. B*, 1996, **54**, 11169-11186.
4. J. P. Perdew, K. Burke and M. Ernzerhof, *Phys. Rev. Lett.*, 1996, **77**, 3865-3868.
5. P. E. Blöchl, *Phys. Rev. B*, 1994, **50**, 17953-17979.
6. H. Li, J. Wang, R. Qi, Y. Hu, J. Zhang, H. Zhao, J. Zhang and Y. Zhao, *Appl. Catal. B*, 2021, **285**, 119778.
7. Y. Lin, P. Liu, E. Velasco, G. Yao, Z. Tian, L. Zhang and L. Chen, *Adv. Mater.*, 2019, **31**, 1808193.
8. L. Zhao, Y. Zhang, L.-B. Huang, X.-Z. Liu, Q.-H. Zhang, C. He, Z.-Y. Wu, L.-J. Zhang, J. Wu, W. Yang, L. Gu, J.-S. Hu and L.-J. Wan, *Nat. Commun.*, 2019, **10**, 1278.
9. L. Jiao, G. Wan, R. Zhang, H. Zhou, S.-H. Yu and H.-L. Jiang, *Angew. Chem. Int. Ed.*, 2018, **57**, 8525-8529.
10. F. Li, G.-F. Han, Y. Bu, H.-J. Noh, J.-P. Jeon, T. J. Shin, S.-J. Kim, Y. Wu, H. Y. Jeong, Z. Fu, Y. Lu and J.-B. Baek, *Angew. Chem. Int. Ed.*, 2020, **59**, 23678-23683.
11. N. Zhang, T. Zhou, M. Chen, H. Feng, R. Yuan, C. a. Zhong, W. Yan, Y. Tian, X. Wu, W. Chu, C. Wu and Y. Xie, *Energy Environ. Sci.*, 2020, **13**, 111-118.
12. X. Zhang, S. Zhang, Y. Yang, L. Wang, Z. Mu, H. Zhu, X. Zhu, H. Xing, H. Xia, B. Huang, J. Li, S. Guo and E. Wang, *Adv. Mater.*, 2020, **32**, 1906905.
13. P. Chen, T. Zhou, L. Xing, K. Xu, Y. Tong, H. Xie, L. Zhang, W. Yan, W. Chu, C. Wu and Y. Xie, *Angew. Chem. Int. Ed.*, 2017, **56**, 610-614.
14. J. Zhang, Y. Zhao, C. Chen, Y.-C. Huang, C.-L. Dong, C.-J. Chen, R.-S. Liu, C. Wang, K. Yan, Y. Li and G. Wang, *J. Am. Chem. Soc.*, 2019, **141**, 20118-20126.
15. J. Li, S. Chen, N. Yang, M. Deng, S. Ibraheem, J. Deng, J. Li, L. Li and Z. Wei, *Angew. Chem. Int. Ed.*, 2019, **58**, 7035-7039.
16. M. Tong, F. Sun, Y. Xie, Y. Wang, Y. Yang, C. Tian, L. Wang and H. Fu, *Angew. Chem. Int. Ed.*, 2021, **60**, 14005-14012.
17. Y. Qu, Z. Li, W. Chen, Y. Lin, T. Yuan, Z. Yang, C. Zhao, J. Wang, C. Zhao, X. Wang, F. Zhou, Z. Zhuang, Y. Wu and Y. Li, *Nat. Catal.*, 2018, **1**, 781-786.
18. G. Yang, J. Zhu, P. Yuan, Y. Hu, G. Qu, B.-A. Lu, X. Xue, H. Yin, W. Cheng, J. Cheng, W. Xu, J. Li, J. Hu, S. Mu and J.-N. Zhang, *Nat. Commun.*, 2021, **12**, 1734.
19. T. Marshall-Roth, N. J. Libretto, A. T. Wrobel, K. J. Anderton, M. L. Pegis, N. D. Ricke, T. V. Voorhis, J. T. Miller and Y. Surendranath, *Nat. Commun.*, 2020, **11**, 5283.
20. C.-C. Hou, L. Zou, L. Sun, K. Zhang, Z. Liu, Y. Li, C. Li, R. Zou, J. Yu and Q. Xu, *Angew. Chem. Int. Ed.*, 2020, **59**, 7384-7389.
21. W. Ye, S. Chen, Y. Lin, L. Yang, S. Chen, X. Zheng, Z. Qi, C. Wang, R. Long, M. Chen, J. Zhu, P. Gao, L. Song, J. Jiang and Y. Xiong, *Chem*, 2019, **5**, 2865-2878.
22. H. T. Chung, D. A. Cullen, D. Higgins, B. T. Sneed, E. F. Holby, K. L. More and P. Zelenay, *Science*, 2017, **357**, 479.
23. J. Li, M. Chen, D. A. Cullen, S. Hwang, M. Wang, B. Li, K. Liu, S. Karakalos, M. Lucero, H. Zhang, C. Lei, H. Xu, G. E. Sterbinsky, Z. Feng, D. Su, K. L. More, G. Wang, Z. Wang and G. Wu, *Nat. Catal.*, 2018, **1**, 935-945.
24. E. Luo, H. Zhang, X. Wang, L. Gao, L. Gong, T. Zhao, Z. Jin, J. Ge, Z. Jiang, C. Liu and W. Xing, *Angew. Chem. Int. Ed.*, 2019, **58**, 12469-12475.

25. F. Luo, A. Roy, L. Silvioli, D. A. Cullen, A. Zitolo, M. T. Sougrati, I. C. Oguz, T. Mineva, D. Teschner, S. Wagner, J. Wen, F. Dionigi, U. I. Kramm, J. Rossmeisl, F. Jaouen and P. Strasser, *Nat. Mater.*, 2020, **19**, 1215-1223.
26. S. Liu, Z. Li, C. Wang, W. Tao, M. Huang, M. Zuo, Y. Yang, K. Yang, L. Zhang, S. Chen, P. Xu and Q. Chen, *Nat. Commun.*, 2020, **11**, 938.